H-SPACE 2022

7th INTERNATIONAL CONFERENCE
ON RESEARCH, TECHNOLOGY AND EDUCATION OF SPACE

Selected papers of 7th International Conference on Research, Technology and Education of Space

April 7-8, 2022, Budapest, Hungary
at Budapest University of Technology and Economics

Organized by
Federated Innovation and Knowledge Centre of
Budapest University of Technology and Economics
and
Hungarian Astronautical Society

Editors
László Bacsárdi and Kálmán Kovács

MANT 2022

Selected papers of the 7th International Conference on Research, Technology and Education of Space (H-SPACE2022)
April 7-8, 2022, Budapest, Hungary
BME building 'I', Hall IE.007 and online
Budapest University of Technology and Economics
Magyar tudósok krt. 2., Budapest, H-1117 Hungary

This publication has been supported by BME VIK, MANT and KKM

Editors: László Bacsárdi and Kálmán Kovács

Publisher (Kiadó):
Hungarian Astronautical Society (MANT, Magyar Asztronautikai Társaság)
1044 Budapest, Ipari park u. 10.
www.mant.hu
Budapest, 2022

Responsible publisher: István Arnócz, Secretary General

This proceeding contains the papers as it was submitted by their authors. We have not edited their text or corrected misspellings.

ISBN 978-963-7367-30-4

WELCOME from the Organizing Committee

In 2022, the International Conference on Research, Technology and Education of Space was held for the 7th time. It was hosted by the BME Space Forum at the Faculty of Electrical Engineering and Informatics of the Budapest University of Technology and Economics (BME) in cooperation with the Hungarian Astronautical Society (MANT).

BME Space Forum is operated by the Faculty of Electrical Engineering and Informatics (VIK) of BME in 2009 to stimulate the research and development activity and to assist the exploitation of research achievements at the Faculty. The mission of BME Space Forum is to harmonize and coordinate space activities in BME by a common vision and strategy, recognize the joint human and technical resources and outstanding achievements, make internal and external knowledge transfer more efficient, and utilize opportunities lying in synergies granted by joint capabilities and unified representation. The common aim of BME Space Forum is to become the bridge between academic research and space industry and participate in the research, the development, the innovation and the application processes of space activity. Currently, 16 Departments from 5 Faculties participate voluntarily in the activities of BME Space Forum.

The Hungarian Astronautical Society (MANT) is a civil organization in Hungary that gathers space researchers, users of space technology, and everyone interested in the interdisciplinary and state-of-the-art uses and research of space. MANT, the oldest space association in Hungary, was established in 1956 in Budapest. It is the only Hungarian member of the International Astronautical Federation (IAF) joining the Federation in 1959. MANT aims to raise public awareness about space activity and space applications. The society also provides an opportunity for space enthusiasts of various fields of sciences to meet, exchange ideas and work together. MANT organizes conferences, youth forums, and summer space camps, issues periodicals, releases media material, and holds lectures about space research and related scientific fields.

The H-SPACE conference series started in 2015, in the year when Hungary became the member of ESA and the grands received as new member increased the opportunities for space activity in Hungary. The Conference also met the needs for a joint presentation of space activities pursued at BME. The conference pays tribute to the successful deployment to orbit the first Hungarian satellite, Masat-1, developed and designed by BME professors and students, was launched on February 13, 2012.

The Hungarian space sector is evolving rapidly. In August 2021, the Hungarian government accepted our national space strategy which is available on the website of the Department for Space Activities of the Hungarian Ministry of Foreign Affairs and Trade at space.kormany.hu. In October 2021, our national astronaut program –the Hungarian in Orbit (HUNOR)– has been announced: Hungary plans to send an astronaut to space in 2024 with Axiom Space. The recently published Hungarian Space Kaleidoscope 2021/2022 contains more than 60 companies, research institutions and university departments working in the Hungarian space sector.
In September 2022, Budapest University of Technology and Economics will start the first class of its space engineering MSc curriculum. In parallel to this, the Ministry of Foreign Affairs and Trade coordinates a nationwide postgraduate education program in four different domains including engineering.

The H-SPACE 2022 conference agenda addressed scientific, technological, and educational issues of space research and space activities. The topic of this year's conference was "New trends in the space sector". The conference was open for both national and international professionals and provides an opportunity to showcase Hungarian scientific, technological, educational, and outreach activities related to space. Due to the generous support of our partners, the conference had no registration fee. The conference was supported by the Ministry of Foreign Affairs and Trade.

Due to the pandemic, we decided to host a hybrid conference. The first day was an in-person day with live stream, the second day was an online day only. We thank the support of the Galileo Webcast for their streaming service.

We had four presentations given by invited speakers:

- *"Space ecosystem building: case study Slovakia"* by Michal Brichta, Head of Industrial Branch of the Slovak Space Office
- *"The effects of the war on the global space policy"* by Balázs Bartóki-Gönczy, Head of Outer Space and Social Sciences Research Center University of Public Services, Hungary.
- *"HUNOR Hungarian Astronaut Program Briefing"* by Balázs Zábori, HUNOR program manager, Centre for Energy Research, Hungary
- *"Space Engineering Curriculum at the Budapest University of Technology and Economics"*, by László Csurgai-Horváth and László Bacsárdi, BME

The conference had four sections:

- Plenary with invited presentations
- Session Science and Technology I
- Session Science and Technology II
- Session Education and Outreach

The Organizing Committee has internationally recognized members: Prof. József Ádám, Dr. Balázs Bartóki-Gönczy, Dr. Tibor Bálint, Ferenc Horvai, Prof. János Lichtenberger, Dr. Lóránt Földváry, Prof. László Pap, Dr. Andrea Pődör, Prof. Gábor Stépán, Dr. Szabolcs Rózsa. We are grateful for their contributions to the success of the conference.

In April 2022, we published a book of abstracts for the conference. In that book, we published all the abstracts of the conference.
During the event, we had four invited lectures and 23 technical presentations. 6 authors of all the presenters submitted a full paper. These papers are included in this conference proceedings

We appreciated all the positive and constructive feed-back from the participants from all aspects. We look forward to organizing the upcoming event of our conference series in 2024.

Dr. László Bacsárdi
co-chair
Vice President of MANT

Dr. Kálmán Kovács
co-chair
President of MANT

Final Conference Program

In this program, the affiliation of the presenter author is listed.

April 7, Thursday

Location: Building I, ground floor, IE.007
Budapest University of Technology and Economics
Magyar tudósok krt. 2., Budapest, H-1117

The first day will be live streamed for online participants.

Session Chair: László Bacsárdi

14:00 Opening ceremony
Orsolya Ferencz, Ministerial Commissioner, Ministry of Foreign Affairs and Trade
Hassan Charaf, Dean, Faculty of Electrical Engineering and Informatics, BME
Kálmán Kovács, President, Hungarian Astronautical Society

14:15 Invited presentation
The effects of the war on the global space policy
Balázs Bartóki-Gönczy, Head of Outer Space and Social Sciences Research Center, University of Public Services, Hungary

14:40 Invited presentation
HUNOR Hungarian Astronaut Program Briefing
Balázs Zábori, HUNOR program manager, *Centre for Energy Research, Hungary*

15:05 Invited presentation
Space ecosystem building: case study Slovakia
Michal Brichta, Head of Industrial Branch of the Slovak Space Office

15:30 Coffee break

Session Chair: Kálmán Kovács

16:00-18:00: Technical presentations – Session Science and Technology I

Experiments on MRC-100 PocketQube
Tibor Herman and Levente Dudás

QO-100 video signal transmitting
Anna Gertrúd Fábián and Róbert Varga

Miniaturized and modular flow chemical reactor for space applications
Ferenc Darvas, Ferenc Boncz, János Takács and Gergő Mezőhegyi

GNSS interference events at Hungarian airports
Bence Takács, Daniel Garcia, Mercedes Reche and Rita Somogyi

Nationwide Ground Motion Map of Hungary Based on Sentinel-1 PSI Data
Péter Farkas, Gyula Grenerczy and Sándor Frey

The Jovian Plasma Dynamics and Composition Analyzer (JDC) - a sensor of the Particle Environmental Package (PEP)
Máté Kerényi, Philipp Wittmann and Martin Wieser

Radio astrometric support for the JUICE mission to Jupiter
Sándor Frey, Judit Fogasy, Krisztina Perger, Krisztina Gabányi and Janka Kőmíves

Hungarian Participation in JUICE Mission of ESA
János Nagy, László Hevesi, Pál Gábor Vizi, Lajos Szalai, István Horváth and Sándor Szalai

April 8, 2022, Friday

Location: online
Registered participants will receive the link for online participation.

Session Chair: László Pap

10:00-12:15: Technical presentations – Session Science and Technology II

Rain Field Sensing Supported by GPS Signal Attenuation
László Csurgai-Horváth, János Bitó, Péter Horváth, Bálint Péter Horváth and Árpád László Makara

Application of Artificial Intelligence in Satellite Communications
Árpád László Makara and László Csurgai-Horváth

Limits of ion-trajectory controll using electric field
András Reichardt, Árpád Makara and László Csurgai-Horváth

A wide-band spectrum monitoring system as a scientific payload for MRC-100 3-PQ(Pocket Qube) student satellite
Yasir Humad and Levente Dudás

InSAR monitoring results of Transcarpathia in the GeoSES Project
Bálint Magyar and Roland Horváth

Using quantum algorithms for Earth Observation data processing
Doaa Subhi and László Bacsárdi

Topic discovery in the diaries of Antarctica winteroverers with multilingual deep sentence encoders
Márton Makrai, Bea Ehmann and László Balázs

Distant Psychological Monitoring of ICE-Groups: Quantitative and Qualitative Content Analysis Approaches
Bea Ehmann, Anna Altbacker, Borbala Tölgyesi and László Balázs

Investigating Cognitive Changes in Space Analog Paradigms
Borbála Tölgyesi, Anna Altbäcker, Irén Barkaszi, Bea Ehmann and László Balázs

12:15- 13:15 Lunch break

Session Chair: Sándor Frey

13:15-15:15: Session Education and Outreach II

Invited presentation
Nationwide cooperation in space education – The UniSpace Hungary Consortium
Bianka Parragh, Programme Director, Head of Space Economy and National Competitiveness Research Group, University of Public Services

Invited presentation
Space Engineering Curriculum at the Budapest University of Technology and Economics
László Csurgai-Horváth and László Bacsárdi, BME

IRF SpaceLab – a Swedish example of opening research infrastructure for external users
Máté Kerényi and Stas Barabash

Székely Mikó T3Ki-rover
Mária Pető

Flórián Vámosi and László Vámosi
Astronomy activities at the Mihaly Tancsics Grammar School of Kaposvar

How Tech Companies can help to Teach Space
Flórián Vámosi, Miksa Vámosi and Andrew Yake

Simulated Mars Rover Model Competition – Years of Pandemic Challenge
Pál Gábor Vizi and Attila Sipos

15:00 Closing remarks

Full Papers

Content

We have published a separate book of abstracts which contains all of the abstracts accepted for the conference. During the conference, we had 4 invited presentations and 23 technical presentations from which 6 authors have submitted a full paper. These papers are included in this proceedings as it was submitted by their authors. We have not edited their text or corrected misspellings.

Rain Field Sensing Supported by GPS Signal Attenuation

László Csurgai-Horváth, János Bitó, Péter Horváth, Bálint Péter Horváth, Árpád László Makara
Department of Broadband Infocommunications and Electromagnetic Theory
Faculty of Electrical Engineering and Informatics
Budapest University of Technology and Economics
Budapest, Hungary
csurgai-horváth.laszlo@vik.bme.hu

***Abstract*—The amount of rainfall over a specific geographical area is an essential factor in agriculture, water management systems, or air traffic control. Still, the design of the sewer network in cities also relies on long-term precipitation data. Radio communications systems also suffer from high signal attenuation, especially in the millimeter wavelength range. The backbone network of the cellular mobile systems or high-frequency satellite communication links is highly attenuated by rainfall. In order to ensure the quality of radio connections is often applied, adaptive technologies are based on instantaneous knowledge of the present weather conditions.**

There are numerous techniques available for rain field sensing. An array of ground-based rain gauges is a simple but device-intensive solution. Among other methods, meteorological radars are widely applied for real-time rain field sensing.

Hydrometeors, especially the rain cause the major part of the attenuation on Earth-space radio links. In ITU-R P.618 the relationship between the rainfall rate and the attenuation can be found up to 55GHz frequencies. With an inverse method by measuring the attenuation, the rainfall rate can be expressed. Thus, satellite radio signals are applied to estimate the cumulated rain intensity over a specific path. If multiple measurements can be performed over different viewing angles, a tomographic method is applicable to reconstruct the rain field structure. The method was also proved with a constellation of geostationary satellites, and the tomographic rain field reconstruction was proved by simulated rain zones over an existing geographical area.

Receiving GPS satellites on medium earth orbit is well applicable for the above-mentioned tomographic rain field reconstruction. These satellites are operating in the UHF frequency band, using code-division multiple access (CDMA) by transmitting pseudo-random (PRN) sequences. The quality of correlation provides sufficient information to estimate the attenuation over the radio path, thus the cumulated rain intensity can also be detected. By passing the satellite on its orbit, different cross-sections of the rain field are scanned, and by using equidistant measurements along with the orbital positions, a tomographic rain field reconstruction can be foreseen.

To prove the concept, software-defined radio based measurements will be performed to test and evaluate the method.

Keywords—rain field; tomography; satellite link; attenuation

I. INTRODUCTION

The distribution of rain intensity and the amount of rain over a specific area and time is important information and has significance in various application areas e.g. in agriculture [1] or in city areas [2], or airports. Millimeter-wavelength terrestrial point-to-point connections, such as the backhaul system of mobile radios, or satellite-earth connections above 10GHz, are also suffering from rain attenuation or rain fading [3].

There are several methods to determine the momentary rain intensity over a specific geographical area. Rain gauges are classical meteorological devices to collect precipitation in the form of liquid water and provide the cumulated rain intensity value for a specific duration [4]. Disdrometers provide some additional information like drop size distribution, while present weather detectors determine precipitation and visibility parameters as well. Weather radar systems are complex and usually costly and consist of a micro-wave transmitter, receiver, and signal-processing unit, and they are suitable for remote sensing of the different precipitation types in the range of several cubic kilometers [5].

A remote sensing method to determine rain intensity based on the measurement of radio wave attenuation between the radio transmitter and receiver was shown for terrestrial point-to-point links in [6] and for satellite connections in [7]. When the path attenuation is known, an inverse power-law expression is applicable to get the rain rate [8].

To visualize a rain field that usually consists of several rain cells with different extensions, accurately measured or sensed point rain intensity values are required. In the literature can be found remote sensing methods based on radio wave attenuation measurements and tomographic rain field reconstruction principles.

Tomography is based on the idea that the cross-sectional image of an object can be reconstructed from several one-dimensional transmission measurements taken from different angles. Therefore, the tomographic method to reconstruct the rainfall field is not a new idea. As radio waves are attenuated when they are crossing a precipitation area, transmission

measurements are feasible by receiving signals from terrestrial or satellite radio sources [9]-[12].

In this paper, we propose the application of GNSS satellite signals in precipitation field remote sensing. This is a passive method; only an appropriate satellite receiver is required, no signal transmission is necessary. We concentrate on GPS satellite constellations as the possible radio signal resources. Considering the permanent availability and the Medium Earth Orbit (MEO) of these satellites, it seems to be an excellent radio source to achieve our goals.

II. GPS Orbits and Signal Properties

Global Positioning System (GPS) is a satellite-based radionavigation system. The full constellation of 24 satellites is orbiting on Medium Earth Orbit at 20.180 km height. Six orbit planes exist with approximately 55° inclination with four satellites each. The orbits are arranged so that at least six satellites are always within line of sight from everywhere on the Earth's surface.

Each GPS satellite continuously broadcasts a navigation message on L1 and L2 frequencies at a rate of 50 bits per second. L1 band at 1575.42 MHz transmits coarse-acquisition C/A and encrypted precision P(Y) codes. For civilians, the C/A code is applicable. L2 and further L3-L5 frequencies are for military and special purposes. Each GPS satellite continuously broadcasts a navigation message, ephemeris data – the precise orbit for the satellite and the almanac, which contains coarse orbit and status information for up to 32 satellites.

All satellites broadcast at the same frequencies, encoding signals using code-division multiple access (CDMA) spread-spectrum technique. The low-bitrate message data is encoded with a high-rate pseudo-random (PRN) sequence that is different for each satellite. The receiver locally reproduces the PRN codes for each satellite to reconstruct the navigation message as Fig. 1 depicts.

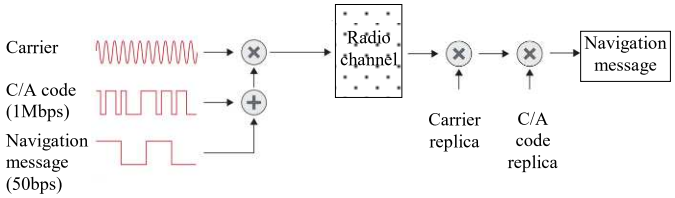

Fig. 1. GPS communication

The CDMA technology allows the successful decoding of the navigation message despite the low received power of the signal transmitted by the satellites. There are different approaches to decode the data stream based on locally generated PRN code and carrier wave to perform cross-correlation with the input signal. The correlation of any two PRN codes from different satellites is low. To determine C/A code, a correlation operation is performed on the incoming signal. In correlation operation, all possible PRN codes are generated as local replicas in the receiver. Then the incoming signal from the satellite is correlated respectively with 37 different PRN codes by shifting the locally generated PRN code in the receiver. When the phase of the GPS receiver replica code matches the phase of the incoming code, there is a maximum correlation.

Atmospheric effects are degrading the quality of the received signal [13], and there are several attempts to apply GNSS signals in remote sensing [14]. Despite the relatively low communications frequency of around 1.5 GHz, there are observable effects showing up in the level of correlation at the GPS receiver side as well. In the next section, we outline the experimental receiver structure that allows investigating the received signal characteristics of the GPS system.

III. A Software Defined Radio Environment for GPS Receiving Qualification

In a software-defined radio (SDR), the typical radio communication system components are implemented by software. The hardware elements, like a superheterodyne RF frontend, followed by an A/D converter, are providing the signal's I/Q samples for further software processing.

In this project, we utilize GNSS-SDR, an open-source environment as a software-defined receiver for global navigation satellite systems [15]. The software provides an interface to different suitable RF frontends and implements all the receiver's chain up to the navigation solution. It allows any kind of customization, including interchangeability of signal sources, signal processing algorithms, interoperability with other systems, output formats, and offers interfaces to all the intermediate signals, parameters, and variables. The software performs signal acquisition and tracking of the available satellite signals, decodes the navigation message, and computes the observables.

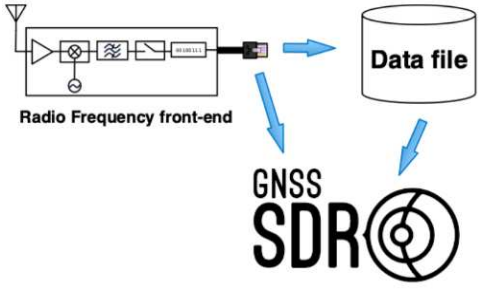

Fig. 2. RF frontend with GNSS-SDR [15]

In GNSS-SDR numerous signal processing blocks are available to perform the different tasks. The acquisition block detects the presence/absence of signals coming from a given GNSS satellite. It provides information about the code phase and Doppler shift. The tracking block follows the evolution of the signal synchronization parameters: phase, Doppler shift, and provides the carrier-to-noise-density ratio, C/N_0, as an indication of the signal quality.

In order to find the relationship between C/N_0 and the atmospheric effects, we intend to apply locally measured weather parameters originating from the weather station of the department. Air temperature, humidity, different wind parameters, and rain intensity values are provided with 1 data/minute resolution.

IV. Tomographic Rain Field Reconstruction

To investigate by screening a three-dimensional object with complex internal structure, tomographic methods are applicable. In the case of absorption tomography, the planar section of a 3D object is screened from different directions, and then the one-dimension records are processed to reconstruct the original planar structure. In the case of the GNSS-based solution, the object is a typical rain field at a specific geographical location, as Fig. 3 shows. A projection of a two-dimensional function (image) is a set of line integrals. The Radon transform computes these line integrals as 1-D projections from multiple sources along parallel paths in a certain direction. By taking multiple parallel-beam projections in the range of 0-180° by rotating the source around the center of the object, a reconstruction of the image of the original object is possible. In this paper, the projections are considered as the path attenuation between a GPS satellite and the ground receiver station.

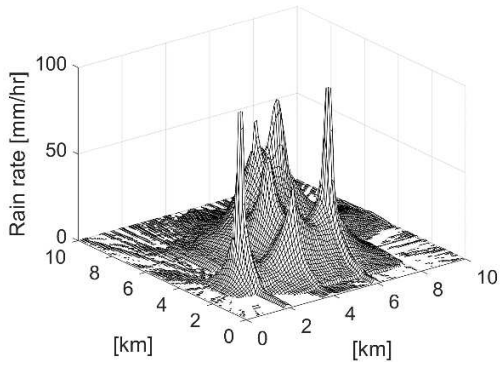

Fig. 3. A typical rain field (simulated with Hycell-model) [12]

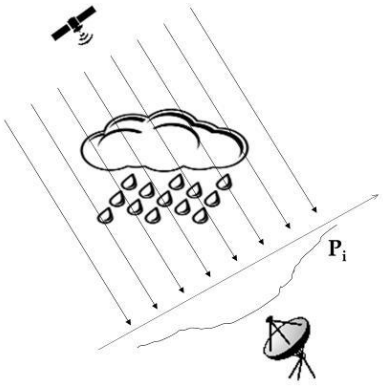

Fig. 4. Parallel-beam projections of the precipitation field

The source is a moving satellite in medium Earth orbit, and the detector is fixed in this case. The individual projections of P_i are measured with equidistant Δt timing, determined by the sampling system of the receiver. With the assumption that the rain field displacement direction and speed do not change significantly during recording the parallel beam projections, a set of consistent data can be measured without introducing distortion in the reconstructed image during the further processing steps.

In the case of the proposed rain-field sensing system, the main advantage is that the overall structure of the station is fixed, moving parts are not required.

The measured attenuation on the satellite-Earth path is the 1 D projection along the slant path L_s and can be expressed as it follows:

$$A_m = L_0 + \int_{l=0}^{Ls} kR(x,y)^{\alpha} dl \quad (1)$$

where $R(x,y)$ represents the rainfall rate value interacting with the link at position (x,y), while k and α are frequency and polarization-dependent constants, L_0 is the clear-sky attenuation value. When the measured radio wave attenuation is A_m, by reversing (1), the estimate of the integrated rain intensity along the path can be determined with (2):

$$A_m = L_0 + \int_{l=0}^{Ls} kR(x,y)^{\alpha} dl \quad (2)$$

The reconstruction of the investigated object is the back-projection, based on the inverse Radon transformation [17]-[18].

A typical rain field reconstruction with inverse Radon-transformation is shown in Fig. 5. In order to create this picture the signal of 12 geostationary satellites are applied over a simulated rain field shown in Fig. 3.

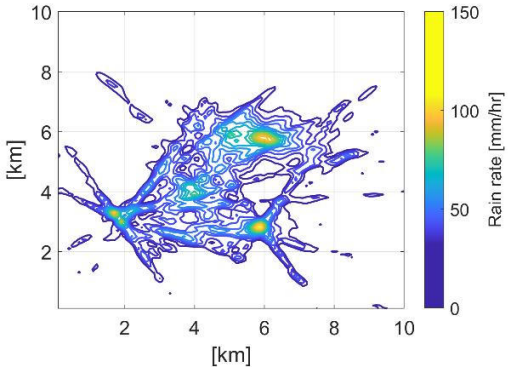

Fig. 5. Reconstructed rain field [12]

Fig. 5 demonstrates that the tomographic rain field reconstruction is a feasible solution when parallel projections of the attenuating medium is available. In the following concluding remarks we summarize the further steps that are necessary to apply the method by utilizing GPS satellite signals.

The visibility duration of a given GPS satellite from a specific ground station is typically 4-7 hours, depending on the orbital plane of the spacecraft. Fig. 6 depicts the 24-hour azimuth-elevation track of the GPS satellites for a specific location. Taking into account that receiving at a very low elevation angle may not be possible, the duration of the recordable time series from a single satellite is still several hours. Considering that at least four satellites are always visible, sufficient remote sensing of a specific rain field is feasible.

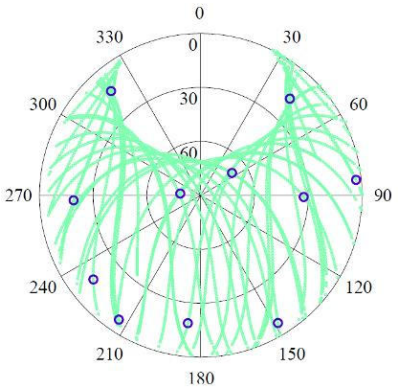

Fig. 6. GPS satellite elevation and azimuth tracks for 24 hours. Satellite positions at a given time are shown with circles [19]

For the proper tomographic image reconstruction of the sensed rain field parallel-beam projections required. This is a strict condition in order to perform high-quality reconstruction. Therefore the geometric correction of the received signal projections will be performed based on the exact knowledge of the satellite positions. This information is included in the navigation message that is transmitted by every GPS satellite and decoded by the applied GNSS-SDR receiver.

V. Conclusions

In this paper, we presented the idea to apply GNSS satellite signals for remote sensing purposes to detect atmospheric effects, especially rain fields. When radio signals are passing the atmosphere from the satellite to the Earth, radio signals are attenuated due to the different precipitation effects. If the radio path crosses the rain field and several projections can be recorded at different viewing angles, inverse-Radon transformation may be applicable to reconstruct the precipitation field. GPS satellites are well applicable for such a purpose, as their visibility is permanent, and by their movement on the MEO orbit different signal paths are crossing the rain zones. If the attenuation is known, the above mentioned tomographic method is applicable.

GPS satellites are utilizing L-band signals for data transmission along with spread spectrum technology. Therefore the path attenuation may be originated from the correlation value of the satellite PRN code. This is a challenging task, and it is our further goal during this research.

References

[1] Torres, M.; Howitt, R.E.; Rodrigues, L.N. Analyzing rainfall effects on agricultural income: Why timing matters. Economica 2019, 20, 1–14.

[2] Cook, L.M.; Vanbriesen, J.M.; Samaras, C. Using rainfall measures to evaluate hydrologic performance of green infrastructure systems under climate change. Sustain. Resilient Infrastruct. 2019, doi:10.1080/23789689.2019.1681819.

[3] Hilt, A. Availability and fade margin calculations for 5G microwave and millimeter-wave anyhaul links. Appl. Sci. 2019, 9, 5240.

[4] Rodda, J.C.; Dixon, H. Rainfall measurement revisited. Weather 2012, 67, 131–136.

[5] Yeary, M.; Cheong, B.L.; Kurdzo, J.M.; Yu, T.; Palmer, R. A brief overview of weather radar technologies and instrumentation. IEEE Instrum. Meas. Mag. 2014, 17, 10–15.

[6] Goldshtein, O.; Messer, H.; Zinevich, A. Rain rate estimation using measurements from commercial telecommunications links. IEEE Trans. Signal Process. 2009, 57, 1616–1625.

[7] Giannetti, F.; Reggiannini, R.; Moretti, M.; Adirosi, E.; Baldini, L.; Facheris, L.; Antonini, A.; Melani, S.; Bacci, G.; Petrolino, A.; et al. Real-time rain rate evaluation via satellite downlink signal attenuation measurement. Sensors 2017, 17, 1864.

[8] ITU. Recommendation ITU-R P.618-13. Propagation Data and Prediction Methods Required for the Design of Earth-Space Telecommunication Systems; ITU: Geneva Switzerland, 2017.

[9] D'Amico, M.; Manzoni, A.; Solazzi, G.L. Use of operational microwave link measurements for the tomographic reconstruction of 2-D maps of accumulated rainfall. IEEE Geosci. Remote Sens. Lett. 2016, 13, 1827–1831.

[10] Giuli, D.; Toccafondi, A.; Gentili, G.B.; Freni, A. Tomographic reconstruction of rainfall fields through microwave attenuation measurements. J. Appl. Meteorol. 1991, 30, 1323–1340.

[11] Cuccoli, F.; Facheris, L.; Gori, S. Radio base network and tomographic processing for real time estimation of the rainfall rate fields. In Proceedings of the IEEE International Geoscience and Remote Sensing Symposium, Cape Town, South Africa, 12–17 July 2009.

[12] Csurgai-Horváth L. Small Scale Rain Field Sensing and Tomographic Reconstruction with Passive Geostationary Satellite Receivers. Remote Sensing. 2020; 12(24):4161.

[13] Mao M., Wang L., Zhang S., Wang X., Hu P. (2017) Correlation Analysis Among GPS-SNR, Precipitation and GPS-PWV. In: Sun J., Liu J., Yang Y., Fan S., Yu W. (eds) China Satellite Navigation Conference (CSNC) 2017 Proceedings: Volume I. CSNC 2017. Lecture Notes in Electrical Engineering, vol 437. Springer, Singapore. https://doi.org/10.1007/978-981-10-4588-2_9

[14] Yu, K., Rizos, C., Burrage, D. et al. An overview of GNSS remote sensing. EURASIP J. Adv. Signal Process. 2014, 134 (2014). https://doi.org/10.1186/1687-6180-2014-134

[15] https://gnss-sdr.org/, accessed on 29.03.2022.

[16] Recommendation ITU-R P.618-13. Propagation data and prediction methods required for the design of Earth-space telecommunication systems. ITU. 2017.

[17] Stanley Roderick Deans. The Radon Transform and Some of Its Applications. Krieger Publishing Company, 1992.

[18] Viergever, Max; Todd-Pokropek, Andrew Eds. Mathematics and Computer Science in Medical Imaging. Springer, 1988.

[19] Ware, Randolph & Alber, Chris & Rocken, Christian & Solheim, Fredrick. (1997). Sensing integrated water vapor along GPS ray paths. Geophysical Research Letters. 24. 417-420. 10.1029/97GL00080.

Application of Artificial Intelligence in Satellite Communications

Árpád László Makara
Department of Broadband Infocommunications and Electromagnetic Theory
Faculty of Electrical Engineering and Informatics
Budapest University of Technology and Economics
Budapest, Hungary
makara.arpadlaszlo@edu.bme.hu

László Csurgai-Horváth
Department of Broadband Infocommunications and Electromagnetic Theory
Faculty of Electrical Engineering and Informatics
Budapest University of Technology and Economics
Budapest, Hungary
csurgai-horvath.horvath@vik.bme.hu

***Abstract*—In connection with satellite-Earth communications the changes in the atmosphere affect the quality of the radio link [1]. For reliable and uninterrupted data transmission the alternating of the modulation and, in many cases, the coding is advantageous. In real-time, these methods are called Adaptive Coding and Modulation Methods (ACM). The most straightforward strategy is to change the coding or modulation if we find that the amount or quality of the transmitted data is inadequate. This means that there may be periods when due to the channel impairments the maximum capacity of the transmission channel can not be achieved.**

The solution to this problem is to predict at least some of the typical transfer quantities. The available solutions are usually regression problems, relying on artificial intelligence to estimate either signal-to-noise ratio or attenuation. There are differences in each technology and the algorithms used, but almost all of them are based on a training method using formal measurements.

In our previous work, we presented a procedure, that performs a new classification method. We do not predict a specific signal-to-noise ratio or attenuation, or the best expected modulation or coding. Our method works acceptably for two-state forecasting, namely the state of fade/non fade. Predictions implemented in this way are expected to perform similarly well with fewer resource requirements than before. In this paper, we present a brief overview of the possible solutions and we perform a comparison of the different methods. The base of the comparison is the conditions of the training of the AI used, its reusability and the possibilities of applying the predicted output.

***Index Terms*—artificial intelligence, satellite communication, deep learning, prediction, ACM**

I. Introduction

Wireless satellite connections are highly weather-dependent, especially at higher frequencies. Adaptive use of transmission capabilities has thus become particularly important in using higher bands. Factors influencing quality can be considered random processes. Nowadays, artificial intelligence research is growing unprecedented, allowing new tools to be deployed.

The current research aims to summarise the main possible applications in satellite communications. These solutions solve or support a kind of adaptive coding and modulation problem using artificial intelligence. Most of the presented methods have been designed for Q-band operation, but they contain considerations and ideas that can be transferred to any band.

At the beginning of the article, the knowledge about artificial intelligence, machine learning (in Sec. II), and neural networks (in Sec. III) is summarised. After concise summaries, a brief introduction to the main considerations of adaptive modulation and coding methods can be found (in Sec. IV).

ACM methods can be read in the second half of the article (from sec. V to Sec. VIII). We present solutions that are functionally based on the published results and assume completely different operations. The sequential procedures use increasingly complex solutions and elements to solve this problem somehow. This arbitrary categorisation does not mean an increase in the number of inputs but the complexity of the algorithms and their training.

Last but not least, a summary of the results can be found in Sec. IX.

II. A Brief Overview of AI and ML

Nowadays, the terms artificial intelligence (AI) and machine learning (ML) are used synonymously. The two concepts are not the same, although they are related to each other. Artificial intelligence is a field of computer science that makes a computer system that can mimic human intelligence [2]. Machine learning is a subfield that enables the machine to learn from past data without being explicitly programmed [2]. Both of them can be divided into more types in several ways. Based on the AI capabilities can be classified this way [2]:

- Weak AI.
- General AI.
- Strong AI.

Also, we can classify the ML techniques based on the nature of the use of the information [3]:

- Supervised machine learning.
- Unsupervised machine learning.
- Reinforcement learning.

In the case of supervised machine learning, the expected response is associated with the input data during training. While in the case of unsupervised machine learning, internal ”rules” are applied instead of the desired response. In the case of reinforcement learning, the algorithm is trained based on

the answer to the ”test information” required during teaching. All three methods can be used alone or in combination (for example, semisupervised machine learning can be achieved through a combination of supervised and unsupervised machine learning) [3].

Each of the methods presented in this article is based on weak AI. They are suitable for one thing, to improve the transmission to satellite communications. However, several ML methods are used in the specific implementation.

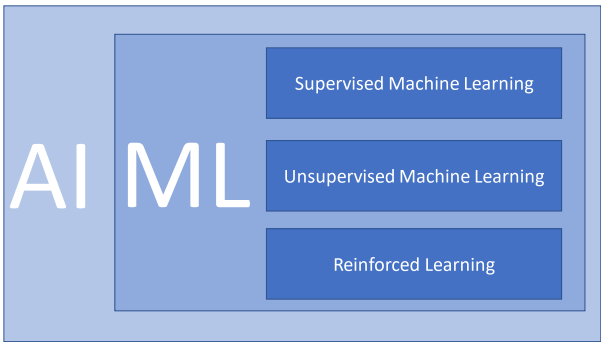

Fig. 1. Relationships between each method.

More commonly used terms are deep learning (DL) and neural network (NN) [3]. While DL stands for possible methods, which are ML procedures that have a hidden layer(s) or element(s), NN stands for a specific algorithm. A neural network is a series of algorithms that endeavours to recognise underlying relationships in a set of data through a process that mimics how the human brain operates [4].

The connections between the main procedures can be seen in Fig. 1.

Two other major task types can be distinguished: classification and regression. In the first case, we expect a discrete class label estimate from the algorithm, while in the second case, we estimate a continuous value quantity. Several problems can be articulated in both ways, and it can be said that classification is usually solved with a smaller model [3].

It can be said that all ML procedures can only be applied to those for whom they have been trained. Therefore, the data used for training determines the usability of the algorithm (this is called the “no free lunch theorem”) [3].

III. Brief Overview of Neural Network and Deep Neural Network

Neural networks are made up of elementary neurons. In the general case, Fig. 2 is shown [5]. The following can be written numerically:

$$a = f\left(\vec{P}\vec{W} + b\right), \tag{1}$$

where a is the output of the neuron, f is the activation function, $\vec{P}$ is the input vector, $\vec{W}$ is the weight vector b is the bias.

A so-called layer can be formed by connecting the individual elemental neurons in parallel. Different structures can be

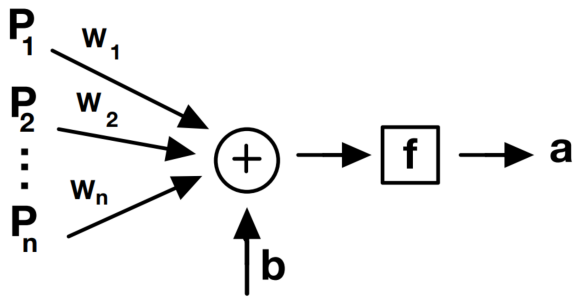

Fig. 2. Multiple-input neuron.

created in each layer in the three most important present cases: fully connected (or dense) [5], LSTM [6] (and other recurrent layers [5]), and convolutional [5].

A fully coupled layer is a simple parallel application of elemental neurons. Recurrent layers contain feedback, thus having memory. The long-short-term memory (LSTM) layer stands out, which has both short-term and long-term memory. These layers are particularly suitable for solving problems where the order of the input data also carries information. The convolutional layer is primarily one of the essential elements of image processing. It takes advantage of the convolutional window size that the data also holds connections and information due to their position.

Neural networks (NN) are often deep neural networks (DNN) because they consist of several layers that already have a layer that has no direct connection to the outside world (by implication, if an NN is not a DNN, it is a shallow NN). In the case of DNN, the feedback of the error to each layer is not trivial, which generates additional problems to be solved. A more detailed presentation of the topic can be found in the referenced literature [4] [5].

IV. Support for Satellite Data Transmission with AI

Broadband satellite communication services require high-speed radio channels. In order for transmission to always be maximal, it is necessary to respond adaptively to environmental changes. This process is called adaptive coding and modulation (ACM). Of course, solutions that only change the modulation (AM) or the coding (AC) are also conceivable.

ACM is both an estimation and a decision problem. An estimation problem is to be understood as it is necessary to estimate at least one of the communication or channel parameters. The decision will be nothing more than a coding or modulation change (usually call it ModCod) based on the estimated values. Since any change in communication requires a finite amount of time, the process has a kind of delay. Thus, on the basis of an estimated value alone, switching is generally not advisable, so either a hysteresis decision or AI should be used. However, not only the decision but also the estimation is AI made typically due to the complexity of the problem.

The two problems can be solved with a common algorithm or even with separate elements (see Fig. 3).

Several previous solutions change ModCod settings along a threshold based on measurable SNR values [7] [8]. These can also be considered weak AI methods, which are built with the help of various classical ML solutions. The receiver station for Alphasat communications experiment, operated at BME, Department of Broadband Infocommunications and Electromagnetic Theory [9], performs the SNR estimation of the received DVB-S2 stream and automatically controls the ModCod of the uplink station. The most important difference from the models now presented is that in these, the model is ready and estimated from current values. While in the models shown, these are developed by a training process on a statistical basis. For this reason, it is also possible to use relationships that we would not fundamentally model.

Of course, there may be a solution to the first type in which one of the components does not contain AI (for example fixed margin methods for ACM [10]).

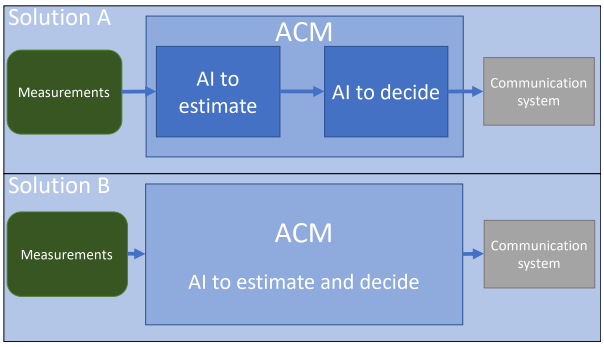

Fig. 3. The two possible solutions with only AI.

The environmental impacts of the transmission can be divided into two parts:

1) From the inaccuracy of the satellite orbit prediction.
2) From changes in channel parameters [11].

Any error in the satellite's orbit or satellite tracking, if known, can be compensated for. In the bands above 10 GHz, the attenuating effect of the atmosphere impairments are increased [12]. ACM is actually used to counteract the effects of these stochastic processes (so that the communication ModCod changes). Of course, the procedures used are also capable of uncompensated first-point errors.

V. ORRF Based ACM

One of the first presented research is a signal-to-noise-ratio (SNR) estimator [10]. Based on the estimated SNR, a DVB-S2 transmitter selects the appropriate ModCod settings [13]. Using the previous designation (Fig. 3) corresponds to type A. The most significant advantage of the procedure is that it estimates the SNR for the future. Based on the attached results, the SNR is estimated with high accuracy and thus performs better than a simple fixed margins method [10]. The researchers worked on real-world measurement results in the Q/V band provided by the Aldo Paraboni experiment on the Alphasat satellite [12].

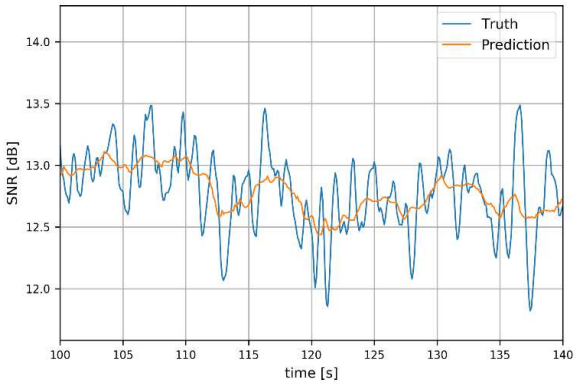

Fig. 4. Results of SNR prediction with ORRF [10].

The algorithm used for estimation is an online random regression forest (ORRF) method [14]. Decision trees decide between their branches depending on the input parameter [15]. The higher the resolution of the terminal leaves (especially in the case of regression), the more branching is required. In the case of regression, the fineness of the resolution is determined by the number of these last leaves. The procedure is essentially a weighted average of decision trees. A major advance in the field has been the solution of online operation (can estimate in real-time), which makes it suitable for the current regression problem. Unfortunately, with the increasing complexity of the forest, the procedure loses its most significant advantage: ease of understanding [16].

The generated ORRF algorithm performs slightly better than the classical methods (see the accuracy in Fig. 4), but its use does not require knowledge of the channel, only the measurement results [10]. A total of one disadvantage can be highlighted, as the size of the trees increases, transparency and maintainability becomes more difficult [16]. The method is easy to apply with less background knowledge than neural networks [3].

VI. DNN Based Fading Estimation with Weather Data

This presented method uses a simple DNN algorithm, but weather data is also used among the input data [17]. During the procedure, the estimated value was the expected attenuation. The air temperature (α), relative humidity (β), rainfall rate (γ), visibility (ϑ), thickness of rainfall amount (φ), average particle diameter (ε), and average particle speed were used (κ). In addition, the previous correct estimate was used in some cases (h'). In each case, the estimated value was the present channel excess attenuation (h). With the markings used, the following four cases were tested [17]:

$$X_1 = [\alpha, \beta, \gamma, \vartheta, \varphi]. \quad (2)$$
$$X_2 = [\alpha, \beta, \gamma, \vartheta, \varphi, h']. \quad (3)$$
$$X_3 = [\alpha, \beta, \gamma, \vartheta, \varphi, \varepsilon, \kappa]. \quad (4)$$
$$X_4 = [\alpha, \beta, \gamma, \vartheta, \varphi, \varepsilon, \kappa, h']. \quad (5)$$

The DNN structure used is built using superficial dense layers without memory. However, there is a significant difference when the previous correct value was also used as an input parameter. The results of feedback-free cases are acceptable on average but cannot predict the exact change. Statistical characteristics of each case and results of the variances interpreted by the measurement results, shown in the Table I. X_2 and X_4 are use previous correct attenuation values.

TABLE I
STATISTICAL ACCURACIES OF EACH CASE. [17]

Statistics \ Input Vector	Measurement	X1	X2	X3	X4
Mean	0.4041	0.4007	0.4079	0.4028	0.4120
Standard Deviation	1.2338	0.9477	1.211	0.9140	1.2075
Correlation Coefficient	1.000	0.7610	0.9549	0.7696	0.9549

Compared to the method presented earlier, the versions with feedback appear to be more accurate; however, more data is required. This means that consecutive data (even at minute resolution) carry information.

VII. Deep Neural Network with Reinforcement Learning for ACM

Apart from all other procedures, this research does not use supervised machine learning but reinforcement learning to accomplish the task [18].

In essence, the procedure is as follows: the transmitter sends a pilot signal to the receiver to estimate the channel state information (CSI). The estimator extracts envelope and phase information from pilot signals. When the channel information is calculated, the phase and envelope are estimated and compensated by the ideal phase discriminator and gain controller. The receiver then sends the CSI back to the transmitter via a feedback path [18]. The channel model used was a Rayleigh-faded model [19].

The structure of DNN was a four-layer fully connected mesh taught using simulation. Several strategies have been used to maximise spectral efficiency. Notably, memory was used outside the main DNN in the structure [18].

The Fig. 5 shows the spectral efficiency results compared to the reference method (blue). It is important to emphasise that maximum efficiency is (by definition) a function of SNR. It is also important to note that the efficiency of the method is minimal under poor conditions.

Although the simulation results are good, there are no comparisons with real measurement results. Thus, the method is as long as the actual cases are largely the same as the ideal model. However, it can be assumed that further improvements are needed before the actual application. The only open question is how fast the algorithm can work in the real case.

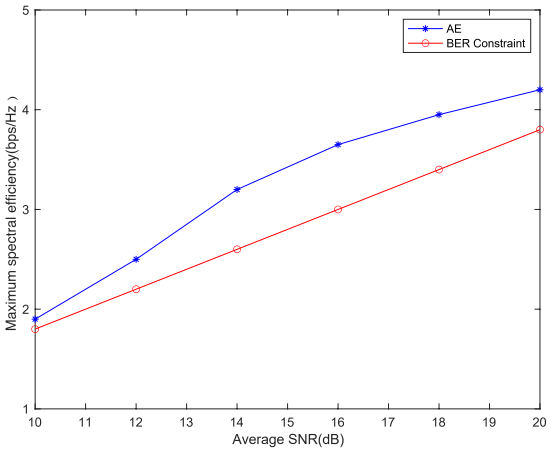

Fig. 5. Maximum spectral efficiency [18].

VIII. AI-Supported Fading Prediction on Q-Band Satellite Channel

Unlike the methods presented earlier, the current solution is a classification [20]. The basic idea of the procedure is that a finite number of ModCod configurations are possible. Thus, with the right amount of training data, a neural network can be created that always selects the correct settings. The procedure is evaluated and decided simultaneously, in one step (type B in Fig. 3). A simplified solution based on binary classification was published in the cited research. However, the advantages and disadvantages of the method are already visible in this case.

The procedure thus actually corresponds to an online fading prediction. The trained neural network with memory (LSTM layer) predicts fading and non-fading events with one-minute time windows [20]. In the case of an ACM implemented in this way, it is necessary to switch between the two modes depending on the forecast. The required data were obtained from the Alphasat satellite experiment [9], which was hand-labelled accordingly. One of the weaknesses of the process is that manual labelling has the potential for error. By implication, for more complex ACM rules, it need to implement labelling using more complex cost functions.

Current results not totally perfect but this can be improved with further investigation. Related results are shown in the Table II. The applied method uses only the results of the measured signal level and the statistical functions interpreted on it as input parameters (average, standard deviation, derivate all of them with moving window).

The great advantage of this method is that it can perform complete ACM tasks in one step. Only the labelling of the training data is the only task to be solved (or fine-tuning the structure of the DNN) so that the task can be performed.

TABLE II
CONFUSION MATRIX RESULTS [20]

Number of LSTM units by layers	50	75	100	150	200	500
Accuracy	93.3%	92.5%	90.7%	92.1%	91.6%	88.3%
Predicted non-fading precision	94.9%	95.3%	96.0%	95.6%	95.4%	96.5%
Predicted fading precision	81.2%	74.6%	64.5%	71.8%	69.6%	58.4%
Specificity	97.4%	96.0%	92.9%	95.2%	94.7%	89.6%
Sensitivity	68.7%	71.4%	77.0%	73.5%	72.7%	80.6%

Retraining the DNN has excellent potential for the general use of such methods.

Another advantage is that the method can work with minimal type of input data.

IX. CONCLUSION

Although the procedures shown are very different, they are all functional. However, it is essential to emphasise that solutions with memory or feedback of the correct value are more accurate. All this means that the temporality of the quantities characteristic of the channel also carries information.

We are of the view that AI-based ACM procedures have great potential for future communication procedures. It can be observed that using multiple types of input data makes it easier to achieve better results. However, with the help of the minimum amount (only the measurable signal level), we can get accurate results by using more complex structures. Thus, in terms of usage, it will be crucial how many sensors and different types of data are available and how much computing capacity can be used to solve the problem.

REFERENCES

[1] "Recommendation ITU-R P.676-12 (08/2019) - Attenuation by atmospheric gases and related effects - P Series -Radiowave propagation," Aug. 2019.

[2] "Difference between Artificial intelligence and Machine learning - Javatpoint." [Online]. Available: https://www.javatpoint.com/difference-between-artificial-intelligence-and-machine-learning

[3] K. P. Murphy, *Machine learning: a probabilistic perspective*, ser. Adaptive computation and machine learning series. Cambridge, MA: MIT Press, 2012.

[4] I. Goodfellow, Y. Bengio, and A. Courville, *Deep Learning*. MIT Press, 2016, http://www.deeplearningbook.org.

[5] M. T. Hagan, H. B. Demuth, M. H. Beale, and O. De Jésus, *Neural network design*, 2nd ed. s.L: Martin T. Hagan, 2014.

[6] S. Hochreiter and J. Schmidhuber, "Long Short-Term Memory," *Neural Computation*, vol. 9, no. 8, pp. 1735–1780, Nov. 1997. [Online]. Available: https://direct.mit.edu/neco/article/9/8/1735-1780/6109

[7] H. Bischl, H. Brandt, T. de Cola, R. De Gaudenzi, E. Eberlein, N. Girault, E. Alberty, S. Lipp, R. Rinaldo, B. Rislow, J. A. Skard, J. Tousch, and G. Ulbricht, "Adaptive coding and modulation for satellite broadband networks: From theory to practice: ACM FOR SATELLITE BROADBAND NETWORKS," *International Journal of Satellite Communications and Networking*, vol. 28, no. 2, pp. 59–111, Mar. 2010. [Online]. Available: https://onlinelibrary.wiley.com/doi/10.1002/sat.932

[8] S. Cioni, R. De Gaudenzi, and R. Rinaldo, "Channel estimation and physical layer adaptation techniques for satellite networks exploiting adaptive coding and modulation," *International Journal of Satellite Communications and Networking*, vol. 26, no. 2, pp. 157–188, Mar. 2008. [Online]. Available: https://onlinelibrary.wiley.com/doi/10.1002/sat.901

[9] L. Csurgai-Horváth, "Receiver station in budapest for q/v band satellite site diversity and adaptive coding and modulation experiments with alphasat," *International Journal of Satellite Communications and Networking*, vol. 37, no. 3, pp. 149–162, 2019. [Online]. Available: https://onlinelibrary.wiley.com/doi/abs/10.1002/sat.1270

[10] J. Ebert, W. Bailer, J. Flavio, K. Plimon, and M. Winter, "A method for acm on q/v-band satellite links based on artificial intelligence," in *2020 10th Advanced Satellite Multimedia Systems Conference and the 16th Signal Processing for Space Communications Workshop (ASMS/SPSC)*, 2020, pp. 1–5.

[11] D. Pozar, *Microwave Engineering, 4th Edition*. Wiley, 2011. [Online]. Available: https://books.google.hu/books?id=JegbAAAAQBAJ

[12] T. Rossi, M. De Sanctis, M. Ruggieri, C. Riva, L. Luini, G. Codispoti, E. Russo, and G. Parca, "Satellite communication and propagation experiments through the alphasat Q/V band Aldo Paraboni technology demonstration payload," *IEEE Aerospace and Electronic Systems Magazine*, vol. 31, no. 3, pp. 18–27, Mar. 2016. [Online]. Available: http://ieeexplore.ieee.org/document/7478406/

[13] "ETSI EN 302 307-1 V1.4.1 - Digital Video Broadcasting (DVB); second generation framing structure, channel coding and modulation systems for Broadcasting, Interactive Services, news Gathering and other broadband satellite applications; part 1: DVB-S2," Nov. 2014. [Online]. Available: https://www.etsi.org/deliver/etsi_en/302300_302399/30230701/01.04.01_60/en_30230701v010401p.pdf

[14] A. Saffari, C. Leistner, J. Santner, M. Godec, and H. Bischof, "On-line random forests," in *2009 IEEE 12th International Conference on Computer Vision Workshops, ICCV Workshops*, 2009, pp. 1393–1400.

[15] J. Quinlan, "Simplifying decision trees," *International Journal of Man-Machine Studies*, vol. 27, no. 3, pp. 221–234, Sep. 1987. [Online]. Available: https://linkinghub.elsevier.com/retrieve/pii/S0020737387800536

[16] T. Hastie, R. Tibshirani, and J. H. Friedman, *The elements of statistical learning: data mining, inference, and prediction: with 200 full-color illustrations*, ser. Springer series in statistics. New York: Springer, 2001.

[17] L. Bai, C.-X. Wang, Q. Xu, S. Ventouras, and G. Goussetis, "Prediction of Channel Excess Attenuation for Satellite Communication Systems at *Q* -Band Using Artificial Neural Network," *IEEE Antennas and Wireless Propagation Letters*, vol. 18, no. 11, pp. 2235–2239, Nov. 2019. [Online]. Available: https://ieeexplore.ieee.org/document/8786170/

[18] Y. Yu and L. Zhang, "Adaptive Modulation Scheme for Satellite Communication Channel Based on RLNN," *Journal of Physics: Conference Series*, vol. 1856, no. 1, p. 012053, Apr. 2021. [Online]. Available: https://iopscience.iop.org/article/10.1088/1742-6596/1856/1/012053

[19] M. K. Simon and M.-S. Alouini, *Digital communication over fading channels: a unified approach to performance analysis*, ser. Wiley series in telecommunications and signal processing. New York: John Wiley & Sons, 2000.

[20] Á. L. Makara, T. Deli, and L. Csurgai-Horváth, "AI-Supported Fading Prediction on Q-Band Satellite Channel," *KA AND BROADBAND COMMUNICATIONS CONFERENCE*, vol. 2021, 2021.

Experiments on MRC-100 PocketQube

Tibor Herman
Budapest University of
Technology and Economics
Budapest, Hungary
Email: herman.tibor@vik.bme.hu

Levente Dudás, PhD
Budapest University of
Technology and Economics
Budapest, Hungary
Email: dudas.levente@vik.bme.hu

***Abstract*—MRC-100 is the upcoming PocketQube mission of BME (TU Budapest) with new and extended measurements and experiments led by András Gschwindt who was the project manager of the previous satellites of BME. It is a 3 unit PocketQube(5x5x17.8 cm) whose primary mission is a wide range spectrum analyser from 30 MHz to 2.6 GHz. To transmit the large amount of data gathered from the measurements, the spacecraft has an S-band transmitter with 30 dBm output power, alongside the VHF telemetry transceiver. To minimize the effects of antenna radiation pattern and thus improve the radio link a redundant attitude determination and control system (ADCS) is implemented. The satellite provides opportunity to several other universities to carry out measurements with their equipment in space.**

Remote sensing such small objects is a challenge for radars that track them around the planet, so orbital predictions show significant inaccuracies compared to larger satellites. To propose a solution for the problem, a new satellite beacon system is described, which provides accurate TLE (Two-line Element) data based on GPS location of the spacecraft.

MRC-100 has an experimental receiver to gather Automatic Identification System (AIS) packets and relay them to the ground station. The system is responsible for tracking vessels and it can improve the coverage where the radio signals do not reach mainland because of the propagation properties of the frequency used.

The project is integrated into the education system as the developers are either university students or lecturers of BME. Guest experiments come from different universities, institutes and companies of Hungary.

I. Introduction

Satellite development in Hungary began with MASAT-1 which was the first Hungarian satellite built by students and lecturers at BME. The mission was successful, exceeding its expectations regarding its lifetime and operating for more than three years [1]. Around the last few months of operation, a part of the team decided to continue satellite development at the university in a new category of nano satellites. The PocketQube was a new idea by prof. Bob Twiggs at Morehead State University at the time. Its goal was to provide a standard for a small, cheaper alternative for CubeSat satellites that can be designed and produced at a low cost using commecial off the shelf components. These satellites could be built by students during their educational course. One unit is one eighth of a CubeSat or 5x5x5 cm and weighs no more than 250 g per unit. [2]

The mission of the SMOG satellites is to measure human caused electromagnetic polltion on LEO (Low Earth Orbit), focusing on the DVB-T (Digital Video Broadcast Terrestrial) band, i.e. 460-860 MHz [3]. Hence the name of the satellite, SMOG-1 (Figure 1). The team consisted of electrical and mechanical engineers students and lectrurers of BME who managed to build two flight models of the SMOG satellites. The launch date of SMOG-1 had already been booked when a second launch opportunity came up, so the second flight model was named SMOG-P (P standing for precursor), because the launch date was earlier than that of its identical pair.

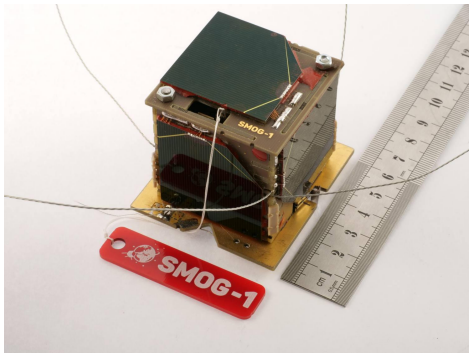

Fig. 1. Flight model of SMOG-1

SMOG-P was launched 6 December 2019, with five other satellites, along with ATL-1 another satellite built by the same team. Of the six PocketQubes only the two Hungarians were operational after deployment, which meant that SMOG-P was the world's first operational PocketQube satellite in space and the second Hungarian satellite. The mission was successful, and with the data gathered from the onboad spectrum analyzer, the first electrosmog map of our planet was created (Figure 2). SMOG-1 was launched 22 March 2021 with a Soyuz-2 rocket and has been operational since then.

II. High level design considerations

A. Mechanical design

MRC-100 is a 3 unit PocketQube with an envelope size of 50x50x178 mm and a maximum weight of 750 g (Figure 3). The mechanical structure of the satellite is made of FR4, which is a standard printed circuit board material, glass-reinforced epoxy laminate [4]. It is durable, flexible and mechanically stable enough to be used as a structural element and this way the area for electronic components is maximized.

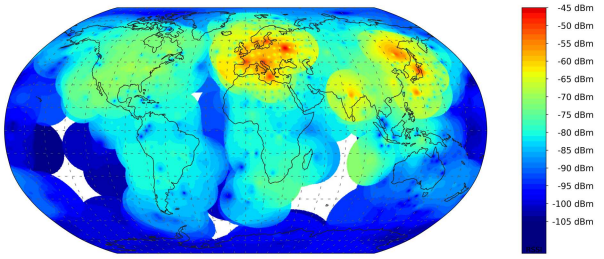

Fig. 2. Electromagnetic pollution map of Earth [5]

The larger outside panels are covered with solar panels which are used to charge the two redundant lithium ion batteries inside. The smaller sides of the PocketQube are used for antennas and a camera. Inside there are 17 PCBs which are connected to the top and bottom panels through 90° connectors (Figure 5).

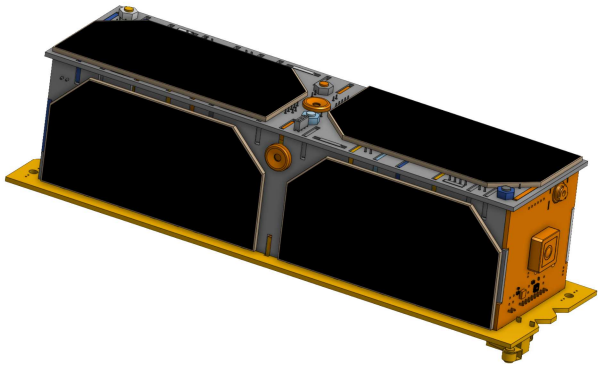

Fig. 3. 3D model of MRC-100

B. Energy budget

In order to avoid the batteries from discharging during the mission, an analysis of power budget is required. To achieve this, the balance of charge and discharge current averaged over a 90 minute orbit has to stay positive. The basic subsystems of the satellite have to be operational cotinuously, however the experiments do not need to be operational all the time, so by duty cycling them the overall consumption can be managed autonomously or remotely. Table I shows the maximum power that each subsystem can consume.

Compared to the consumption the available power delivered to the batteries is estimated in a worst case scenario. This happens when only one side of satellite is in sunlight (apart from the small sides without solar cells). The solar power density in space is $1360\frac{W}{m^2}$. Using 3 layer 80x40 mm GaAs cells with 29% efficiency [6] the output power is 1.26 W, each. That is a total of 2.52 W per side. Considering the time the satellite spends in sunlight during an orbit, the average power delivered to the batteries is at least $0.6 \cdot 2.52W = 1.52W$. It is clear that the duty cycling the non-essential subsystems is necessary to maintain a positive balance of the energy flow.

TABLE I
ENERGY CONSUMPTION OF EACH SUBSYSTEM

Subsystem	**Max. power [mW]**
OBC	100
EPS	60
COM	500
Spectrum analyser 1	330
Spectrum analyser 2	330
Sun and horizon sensor	300
Magnetic and gyro sensor	80
Attitude control	660
Camera	500
GPS	230
AIS receiver	66
S-band transmitter	2200
5 additional eperiments	825
SUM	**6182**

C. Communication

The design of the radio communication link is a crucial aspect of the mission. In order to have a reliable link that is closed during the complete pass over the ground station a link budget calculation is done that shows the signal-to-noise ratio margin for a given set of parameters.

TABLE II
DOWNINK BUDGET CALCULATION [7]

Frequency	437 MHz
Wavelength	0.69 m
Distance at horizon	2830 km
Transmit power	20 dBm
Transmit antenna gain	0 dB
Path loss	154 dB
Receiver antenna gain	25 dB
Polarization loss	3.3 dB
Atmoshperic and Ionospheric losses	5.4 dB
Receiver losses	4.7 dB
Signal power at receiver	-122.4 dBm
Data rate	5000 bps
GMSK bandwidth	7500 Hz
Thermal noise level	-133 dBm
Signal to noise ratio	10.6 dB
$E_b/N_o(SNR * B/R_b)$	12.3 dB
E_b/N_o threshold for (10^{-5}) BER	6 dB
Link margin	**6.3 dB**

In Table II a 5000 bps GMSK modulation is assumed as the default scheme for the downlink telemetry. The link is assumed to be closed if the bit error rate is below 10^{-5}, which is provided if E_b/N_0 is greater than 6 dB. The path loss and thermal noise level are calculated by Equations 1 and 2 respectively. On a 600 km orbit at 0° elevation the slant range is 2830 km, where the available margin is 6.3 dB, so the link is closed at all times using the 4.5 m parabolic antenna at the ground station of the univerity.

The uplink uses the same parameters except for the output power, which can be scaled from 100 W to 1000 w which is 3-4 orders of magnitude higher than the dowlink transmit power. For this reason the uplink budget is not calculated separately.

$$a_0 = 10lg\left(\frac{4\pi d}{\lambda}\right)^2 \quad (1)$$

$$P_n = 10lg\,(kTB) \quad (2)$$

D. Basic subsystems

The basic subsystems of the satellite are designed to be fault tolerant, meaning that all of them are redundant. In case of a fault event onboard, the satellite can switch to the redundant pair of the faulty module, which is by experience a game changer feature. Looking at the telemetry data of SMOG-P and SMOG-1 we can see that switches over to the spare module happened several times, which could have been caused by either an overcurrent, overvoltage or even a single event latchup. If the problem can be fixed by a reset then the primary module can be used later when another fault occours in the active system [8].

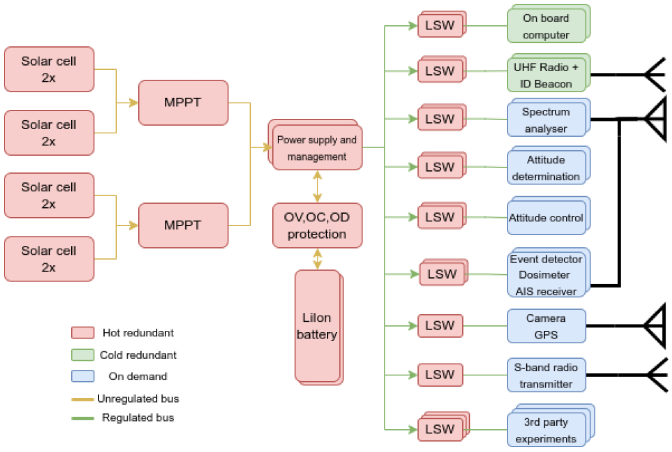

Fig. 4. Block diagram of MRC-100 electronics

E. Attitude determination and control

The patch antenna on the S-band transmitter (Subsection III-B) is a directional antenna with some gain, so it is desirable for its main direction of radiation to be pointed at the ground station of MRC-100. This requirement makes the use of some form of attitude control a must. There are several ways to determine and control the orientation of a satellite in a Low Earth Orbit.

1) Sensors: Without claiming completeness the determination can be done with motion sensors, star tracker, horizon sensor, magnetometers, gyroscopes, etc. There are four types of sensors in the satellite to determine its attitude: 3-axis magnetometer, 3-axis gyroscope, a coarse light sensor, one on every side of the satellite and four MLX90640 far infrared thermal sensor arrays with 32x24 pixel resolution, which is used as a Sun and horizon sensor [9].

2) Actuator: Actuation can also be achieved with different techniques like using magnetorquers, thrusters, momentum wheels just to name a few. Due to size and power limitations regarding actuation, magnetorquer actuation was selected, because it can be used on LEO interacting with Earth's magnetic field, does not contain moving parts, it has low power consumption and it is easy to manufacture the required coils in small size. Although its pointing accuracy is not as good as the other methods', however for the relatively wide beam of the patch antenna its theoretical approx. 1° is sufficient [10].

Magnetorquers can be created in several forms. To generate a magnetic dipole of arbitrary vector direction, three orthogonal electromagnets have to be constructed. They can be air(vacuum) core coils, solenoids with metal cores, coils made of embedded copper traces on a PCB. To maximize magnetic torque two of the coils are metal core solenoids and the third is a vacuum core coil that occupies the most space available. Because the subsystem is redundant, there are two identical sets of coils in the satellite and they can be used in two ways: simultaneously generating larger magnetic torque or separately as each other's replacement to save energy.

Since the most complicated system on the satellite is the attitude determination, it has the exclusive feature of over the air updates of its firmware. This way the control algorithm can be tested and debugged on Earth and new versions can be deployed on the active satellite in space.

The three coils are manufactured by the author using 3D printing technology and custom machined metal cores. They are used in a H-bridge configuration and the electronic control of the actuators is done with a PIC18F27 microcontroller. The controller has built-in H-bridge controller that guarantees that there is no short circuit caused by two serial transistors conducting at the same time and the coil current can be controlled by pulse modulation techniques [11].

III. Scientific Payloads

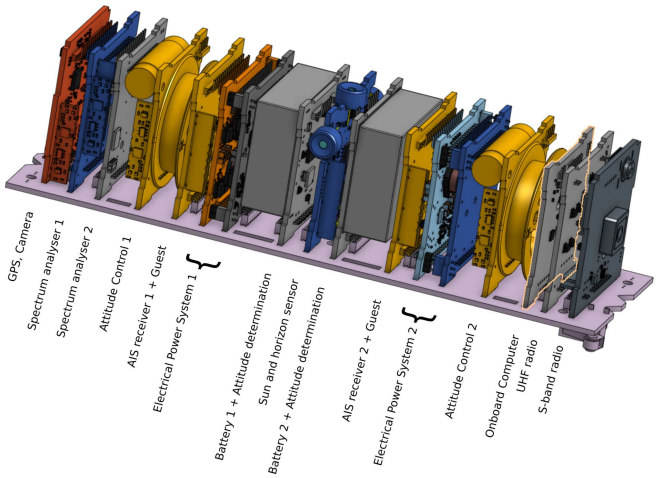

Fig. 5. Internal structure and subsystems of MRC-100

A. Spectrum analyser

The primary experiment of the mission is the broadband spectrum analyser, which is a redundant, fault tolerant subsystem of the satellite. The measurement antenna is a calibrated dipole made of stainless steel that is salvaged from brake cable of a bicycle. It is a durable, solderable and very flexible and has proven to be a quite reliable antenna material, because it regains its original shape after several wrappings and deployments.

The measurement electronics use two different approaches, although both of them use a single chip radio receiver. The primary module is uses the Silicon Labs Si4464 radio transciever. It is used as a receiver in the range between 119 and 960 MHz [12]. In order to extend its frequency range a frequency mixer is used. The antenna input can be connected to four different bandpass filters. The filtered inputs are then amplified in and a single frequency (both up and down) conversion can take place with a double balanced mixer if the frequency of interest is outisde the transciever's band. Then another bandpass filter is applied to the signal to suppress the mirror frequency components introduced by the conversion. Finally the receiver sweeps the band of interest and records the RSSI (Received Signal Strength Indicator) value, that is stored in the onboard computer [14].

The secondary analyser uses another single chip transciever by Silicon Labs, EFR32MG24, which can be tuned between 93 and 2600 MHz with a gap between 1000 and 1100 MHz. The same RSSI reading method is used with this radio, but since it is capable of sweeping almost the whole frequency range, it has no other input stages than the radio itself.

Since both analysers use the same antenna, RF PIN (Positive Intrinsic Negative) diodes are used to route the radio signal to the necessary subsystem. Moreover, the antenna is used not only by the two spectrum analysers, but it is used by the AIS receivers, as well.

B. S-band transmitter

Since the wide spectrum measurement bandwidth generates a significant amount of data, a high speed downlink transciever is designed. The maximum 12.5 kbit/s data rate of the telemetry transmitter with an omnidirectional antenna can become a bottleneck in the data throughput, so MRC-100 has a GMSK transmitter whose uncoded data rate is at least an order of magnitude higher and works in the professional S-band around 2.2 GHz. The target speed is 1 Mbit/s, which is achieved with an EFR32MG module. The output of the radio is connected to a power amplifier which generates a 27 dBm RF signal that is radiated by a linearly polarized patch antenna with about 4 dBi gain and is placed on one of the smaller sides of the 3 unit PocketQube.

The transmitter is a redundant, fault tolerant subsystem of the satellite with a shared antenna that is connected through an RF switch.

C. GPS based low power satellite identification beacon

Objects in space are observed and tracked by remote sensing technology by NORAD (North American Aerospace Defense Command) and orbit data, called TLE (Two Line Element) is generated for each of them which can be used for orbit prediction. Satellites are typically measured once or twice a day and with every measurement the TLE becomes more and more reliable. It is a fundamental information when it comes to tracking satellites, because it not only gives information about the location of the object, but the doppler frequency can be calculated with it, which is necessary apriori knowledge for the demodulation of the telemetry data and also for transmitting telecommands. Usually, during the first few days of a satellite mission the prediction can be inaccurate, especially in the case of PocketQubes or other smaller satellites, which might have a shorter orbital lifespan measured in weeks if they are put on lower orbits. In these cases it is important to gather as much telemetry data as possible in a short time, so having an accurate TLE is very important.

Using a GPS receiver that works in LEO solves this issue, if the information can be collected early in the mission. MRC-100 has a wideband transmitter, that uses spread spectrum (LoRa) technology that is robust in terms of frequency error, sacrificing data rate [15]. Since the information that needs to be transmitted is very small (16 bytes is sufficient) this tradeoff is worth it. Another advantage of the technology is that the packets can be received with a simple dipole antenna and a cheap receiver.

D. AIS receiver

The AIS (Automatic Identification System) is a self organizing vessel tracking system which uses short FSK modulated data packets that are transmitted on two channels 25 kHz over and under 162 MHz. Due to the horizon limitations the range of a packet on the surface is about 74 kilometres, so vessels that are further away from the coast cannot be directly seen by the coastal receivers [17]. However, as this frequency is able to propagate through Earth's atmosphere, the range can be much more towards space. A suitable receiver on a LEO satellite is able to receive these packets and relay it back to Earth, so MRC-100 has a dedicated radio that can receive the packets sent by the transmitters. The problem that needs to be addressed is the message collisions caused by the large footprint of the receiver antenna. The AIS standard has 4500 available time-slots each minute, but it can be overloaded with the increased area that the receiver sees.

There exist a number of satellites that are used as relays for AIS packets, however they are larger micro satellites. AAUSAt-3 was an experimental 1U Cubesat that was operational in 2014 [16], however since then no other small satellite missions carried this kind of experiment on board.

The experiment this time is not a real time relaying function but rather the research of the possibility to realize the function on such small satellite, which could significantly reduce the costs of operating S-AIS (Satellite-AIS).

E. Guest experiments

MRC-100 provides opportunity for several universities along with some companies to test their scientific experiments in space. The payloads include Sun and Earth horizon sensors by Konkoly Observatory, a RAM based event detector by the University of Debrecen, a compact total ionizing dose measurement by 27G-Technology Kft., a thermal insulation material experiment by H-ION Kft. and further experiments by the University of Szeged, University of Óbuda and Széchenyi István University.

IV. Conclusion

In this paper the brief history of satellite development at TU Budapest was discussed. The mission of MRC-100 is described, focusing on high level design considerations, basic subsystems and the scientific payloads. At the time of writing, active development of the satellite is in progress. Further work is required to integrate the system as a whole and to complete the qualification tests that are required for the launch broker.

Acknowledgment

Prepared with the professional support of the Doctoral Student Scholarship Program of the Co-operative Doctoral Program of the Ministry for Innovation and Technology from the source of the National Research, Development and Innovation Fund.

References

[1] L. Dudás, L. Pápay and R. Seller, "Automated and remote controlled ground station of Masat-1, the first Hungarian satellite," 2014 24th International Conference Radioelektronika, 2014, pp. 1-4, doi: 10.1109/Radioelek.2014.6828410.

[2] https://en.wikipedia.org/wiki/PocketQube (Accessed April 6, 2022)

[3] L. Dudás, L. Szűcs and A. Gschwindt, "The spectrum monitoring system by Smog-1 satellite," 2015 Conference on Microwave Techniques (COMITE), 2015, pp. 1-4, doi: 10.1109/COMITE.2015.7120316.

[4] https://www.eurocircuits.com/fr-4-fiberglass-reinforced-flame-retardant-base-material/

[5] D. Takács, B. Markotics, and L. Dudás, "Processing and Visualizing the Low Earth Orbit Radio Frequency Spectrum Measurement Results From the SMOG Satellite Project," *Infocommunications journal*, vol. 13, no. 1, pp. 18–25, 2021, doi: 10.36244/icj.2021.1.3.

[6] AzurSpace solar cell datasheet, http://www.azurspace.com/images/0003429-01-01_DB_3G30C-Advanced.pdf (Accessed April 6, 2022)

[7] Link budget calculator: https://amsat-uk.org/tag/link-budget/ (Accessed April 6, 2022)

[8] http://gnd.bme.hu/smog1status (Accessed April 6, 2022)

[9] Datasheet of MLX60640. https://media.melexis.com/-/media/files/documents/datasheets/mlx90640-datasheet-melexis.pdf (Accessed April 6, 2022)

[10] N. Sugimura, T. Kuwahara and K. Yoshida, *"Attitude determination and control system for nadir pointing using magnetorquer and magnetometer,"* 2016 IEEE Aerospace Conference, 2016, pp. 1-12, doi: 10.1109/AERO.2016.7500665.

[11] Datasheet of PIC18F27. https://ww1.microchip.com/downloads/en/DeviceDoc/PIC18F27-47-57Q43-Data-Sheet-40002147F.pdf (Accessed April 6, 2022)

[12] Datasheet of Si446x. https://www.silabs.com/documents/public/data-sheets/Si4464-63-61-60.pdf (Accessed April 6, 2022)

[13] Datasheet of EFR32MG24. https://www.silabs.com/documents/public/data-shorts/efr32mg24-datashort.pdf (Accessed April 6, 2022)

[14] Nagy Dominik Gábor. *Műholdfedélzeti szélessávú spektrumanalizátor fejlesztése.* BSc Thesis, Budapest University of Technology and Economics, 2021.

[15] Petäjäjärvi J, Mikhaylov K, Pettissalo M, Janhunen J, Iinatti J. *Performance of a low-power wide-area network based on LoRa technology: Doppler robustness, scalability, and coverage.* International Journal of Distributed Sensor Networks. March 2017. doi:10.1177/1550147717699412

[16] AAUSAt-3,https://directory.eoportal.org/web/eoportal/satellite-missions/a/aausat3 (Accessed April 6, 2022)

[17] S. Bhattacharjee, *"Automatic Identification System (AIS): Integrating and Identifying Marine Communication Channels,"* Marine Insight, Mar. 27, 2021. https://www.marineinsight.com/marine-navigation/automatic-identification-system-ais-integrating-and-identifying-marine-communication-channels/ (Accessed April 6, 2022)

A wide-band Spectrum Monitoring System as a Scientific Payload for MRC-100 3-PQ(Pocket Qube) Student Satellite

1st Yasir Ahmed Idris Humad, 2nd Levente Dudás
Dept. of Broadband Infocommunications and Electromagnetic Theory,
Faculty of Electrical Engineering and Informatics
Budapest University of Technology and Economics (BME), Budapest, Hungary
yasirahmedidris.humad@edu.bme.hu, dudas.levente@vik.bme.hu

***Abstract*—The main aim of this paper is to present the capability of designing 3-PQ (Pocket Qube) student satellites for scientific payloads with limited size, weight, and power consumption. The planned scientific payload of MRC-100 is a wide-band spectrum monitoring system(30 – 2600) MHz This system is able to measure the upper HF band, VHF band, UHF band,5G band, 4G band, GSM band, and UMTS band at the laboratory environment as a prototype (first phase). The realized prototype panel of the spectrum monitoring system is now working, is able to measure RSSI (Received Signal Strength Indicator) values on three different RF bands, it can be used as a conventional scalar spectrum analyzer with less than 120 mA current consumption from +3.3 V nominal regulated bus voltage and 40mm × 40mm PCB (Printed Circuit Board) size.**

***Index Terms*—Student Satellite, PocketQube, Radio Frequency Smog, Spectrum Monitoring System.**

I. Introduction

MRC-100 (5 × 5 × 15)cm is a 3-PQ (PocketQube) class student satellite with a total mass of 750 grams. MRC-100 is being explored as a possible continuation of SMOG-P, ATL-1 and SMOG-1 as 2nd , 3rd and 4th Hungarian PocketQube class satellites integrated to the educational system of BME, made by university students. SMOG-P was the first, smallest ((5 × 5 × 5)cm, 183 g mass) operational satellite in the world at the time of its launch (2019-12-06) with scientific payload on-board: the public DVB-T (digital video broadcasting terrestrial) band spectrum monitoring system (electromagnetic pollution measurement). [1]. [6]. [8].The main subsystems of MRC-100 are: EPS - Electrical Power System, OBC - On-Board Computer, COM - Communication System. There are several payloads on-board the satellite: spectrum analyzer (30 - 2600 MHz), active magnetic attitude control, horizon + Sun camera, satellite GPS + LoRa downlink (satellite identification), 1 Mbit/s S-band down-link, total ionizing dose measurement system, automatic identification system receiver for vessel traffic services, UHF-band LoRa-GPS Tracking, memory based single event detector, special thermal insulator test. The 3D model of MRC-100 student satellite can be seen in Fig.1 .

The proposed trajectory for the MRC-100 is a polar, circular and sun-syncronous Low Earth Orbit (LEO) with distance of 600 km apogee and perigee.

The distance between Sun and Earth is about 150 million km. Around the Earth, the averaged power density equals to $1360\frac{W}{m^2}$ [2]. MRC-100 will be covered by solar panels made by AzurSpace [3]: 8 pieces of three-layers 80×40 mm cells.

The solar power density on Earth's surface is only $1000\frac{W}{m^2}$ due to the atmosphere (mainly by the ozone layer) [5]. The three-layer solar cells of the MRC-100 have a 28% efficiency and a $40mm \times 80mm$ dimension, resulting in a DC (Direct Current) power of 1.1 W. MRC- 100's LEO lasts 90 minutes, with 60% in the light and 40% in the dark. As a result, the averaged DC input is 0.68 W, with 1.7 W peak (on LEO DC input will be 36% more). MRC-100 will have single-point-failure tolerant and cold-redundant on-board systems.

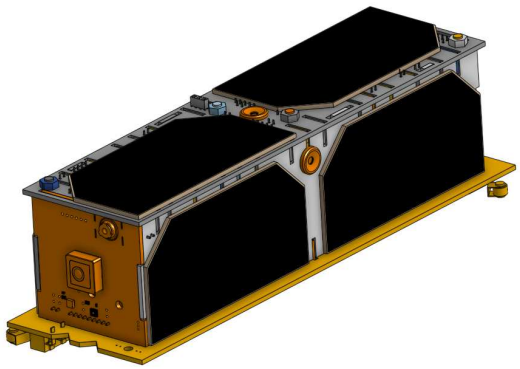

Fig. 1: MRC-100 3D model

II. The Main Sub-Systems of MRC-100

- EPS: The 3-PQ surface is covered by solar panels. The EPS primary responsibilities are to autonomously control the operating point of the solar panels in order to achieve maximum input DC power, charge the Li-Ion bettery cell in order to work on the dark side of the Earth, and supply a stable +3.3 V regulated bus voltage to the other subsystems.
- OBC: controls the operation of the on-board electronics as COM (communication system) and the payloads. The OBC is responsible for the on-board data collection and handling (these data will be the radiated telemetry data by COM).
- COM: is responsible for establishing a two-way data link between the satellite and the ground stations. Because of the size of the on-board antenna, which must be opened from the cube, this radio transmission is running on the 70 cm UHF radio amateur band (437 MHz nominally).

III. The Main Payload of the MRC-100 Satellite

The MRC-100's main payload will be a wide-band spectrum monitoring system. A single-chip radio transceiver (in receiver mode) from Silicon Laboratories SI 4464 is used to monitor the spectrum. This receiver has a frequency range of 119 to 960 MHz with a bandwidth from 1 to 850 kHz [4]. The frequency band being monitored is 30 to 1800 MHz. The single-chip transceiver's block scheme (SI4464) is in Fig.2.

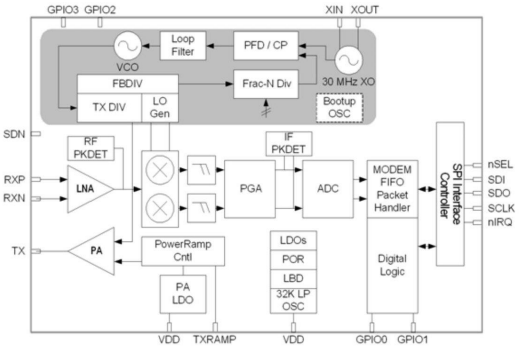

Fig. 2: Single-chip radio transceiver as a spectrum monitor.

This transceiver's receiver is a standard superheterodyne receiver with a digital IF (Intermediate Frequency) unit. The SI4464 chip has a wide-range fractional-PLL (Phase Locked Loop) as a local oscillator, a wide-band LNA (Low Noise Amplifier) and mixer, PGA (Programmable Gain Amplifier) as an IF amplifier with low pass filter, I-Q ADCs (Analogue to Digital Converters), and digital OOK-FSK MO-DEM as a digital OOK-FSK MO-DE (Modulator and Demodulator) [4].The task of the spectrum monitor is to tune the receiver's carrier frequency from 119 to 960 MHz and read the RSSI (Received Signal Strength Indicator) register values of the receiver chip. With fractional-PLL(Phase Locked Loop), the Locked frequencies and the frequencies gab of the local oscillator is shown in Fig.3.

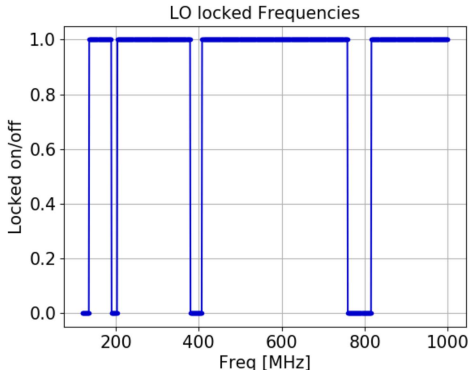

Fig. 3: SI1060 as Local Oscillator.

IV. WideBand Spectrum Monitoring System

The main payload of MRC-100 will be a wide-band spectrum monitoring system 40mm × 40mm dimension, on the upper HF band, FM band, VHF band, UHF band, 5G band, GSM band, and UMTS band (30 to 1800) MHz frequency range. The MRC-100's spectrum monitoring system is based on an RF microcontroller from Silabs SI1060. It contains a SI4464 digital radio module and a C8051F930 micro-controller in a single Quad Flat No-Lead (QFN) package. Fig.4. shows the experimental model of the MRC-100's spectrum monitoring system.

As shown in Fig.4 . There are several electronic components TCXOs (temperature compensated crystal oscillators) as a reference oscillator, and (SI 4464) as a radio transceiver chip is on the right up. the RF switches, an active mixer, and an LNA (Gain Block Amplifier) in the middle. The monopole antenna connection for the three sub-bands in the left and the frequency multiplier in the left down.

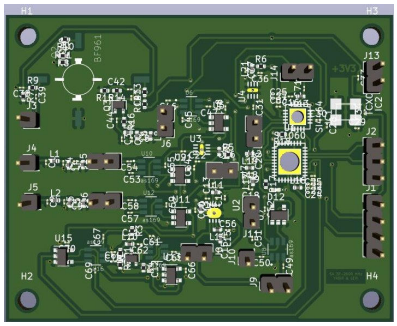

Fig. 4: The PCB of The Experimental Model.

The above-mentioned transceiver's receiver side (SI4464) can operate in RF scanning mode. The SI4464 chip measures the RSSI (Received Signal Strength Indicator) level with

enough dynamic range and 1 dB accuracy at a given frequency and bandwidth. This wideband (30-1800MHz) must be divided into sub-bands based on the chip operating frequency range (119-960)MHz.

A. First Band From 30MHz to 119MHz

The task in the case of the first band is to adjust the receiver carrier frequency from 119 to 960 MHz and read the values from the receiver chip's RSSI register (Received Signal Strength Indicator), but the first band frequencies are lower than the receiver chip's range. As a result, the received signal is up-converted to the frequency range of the receiver chip by tuning the local oscillator to 820MHz. To filter the first band signals, the monopole antenna is connected directly to the RF BPF (Band Pass Filter) controlled by the first RF Switch stage.

B. Second Band From 119MHz to 960 MHz

The task in the case of the second band is to adjust the receiver carrier frequency from 119 to 960 MHz and read the values from the receiver chip's RSSI register (Received Signal Strength Indicator) Because the second band's frequencies are within the receiver chip's range, the monopole antenna is connected directly to the IF BPF (Band Pass Filter) controlled by the second RF Switch stage in order to filter the second band signals.

C. Third Band From 960MHz to 1800 MHz

The task in the case of the third band is to adjust the receiver carrier frequency from 119 to 960 MHz and read the values from the receiver chip's RSSI register (Received Signal Strength Indicator) but the third band frequencies are lower than the receiver chip's range. As a result, the received signal is down-converted to the frequency range of the receiver chip by tuning the local oscillator to 841MHz. To filter the third band signals, the monopole antenna is connected directly to the RF BPF (Band Pass Filter) controlled by the third RF Switch stage.

The antenna of the wideband spectrum monitoring system is a 470 mm monopole used in a wide frequency range without a matching circuit. The differential input impedance of the receiver is 450 ohm parallel with 10 nF over a wide frequency range. As a result, the measurement monopole antenna is directly connected to the RF BPF (Band Pass Filter) in the first and third bands but is connected directly to the IF BPF (Band Pass Filter) in the second band. Fig.5. shows the Antenna on-board cube-skeleton and it is radiation pattern with 45 degrees.

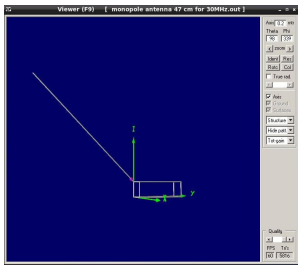

(a) Antenna on-board cube-skeleton.

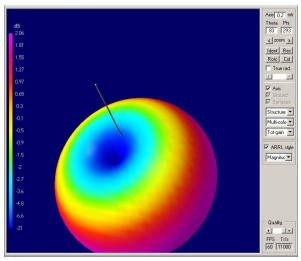

(b) Three dimensional radiation pattern of the antenna with 45 degree.

Fig. 5: 2 Figures Antenna on-board cube-skeleton and it is radiation pattern with 45 degrees.

V. SPECTRUM MEASUREMENT RESULTS

The wide band spectrum monitoring system of MRC-100 satellite was tested at the laboratory environment as a prototype (first phase) to monitor signal levels in the upper HF band, FM band, VHF band, UHF band, LTE band, GSM band, 4G band, and UMTS band.

The used bandwidth of the receiver chip is 800 kHz (maximal bandwidth of the chip is 850 kHz), controlled by the configuration software. the measurement minimum time for each band must be calculated; the minimal time is determined by the Resolution Bandwidth (RBW) and Step Frequency as shown in table.I.

$$MinimalTime = \frac{f_{\max} - f_{\min}}{f_{step}} \cdot \frac{1}{RBW} \cdot 10 \tag{1}$$

$$DataRate_{GMSK} = 2^{RBW} \tag{2}$$

$$RBW = 1.5 \cdot DataRate \tag{3}$$

$$StepFrequency = \frac{RBW}{4} \tag{4}$$

TABLE I: The Minimal Time of Band Scanning.

Band	RBW KHz	GMSK(DR) kb/s	Step Frequency kHz	Minimal Time [S]
FM	192	128	48	0.022
DVB-T	192	128	48	0.009
LTE	192	128	48	0.011
4G	192	128	48	0.022
GSM	192	128	48	0.048
UMTS	192	128	48	0.005

The total measurement points of the wideband spectrum (30 - 1800)MHz, when the Resolution Bandwidth (RBW) is 192 kHz and the f_{step} is 48 kHz can be calculated by equation 5.

$$TotalPoints = \frac{f_{\max} - f_{\min}}{f_{step}} = 36875 points \quad (5)$$

The minimum time of measuring the RSSI values of the wideband spectrum(30 - 1800)MHz, when the Resolution Bandwidth (RBW) is 192 kHz and the Step Frequency is 48 kHz can be estimated by equation 6.

$$Mini.Time = TotalPoints \cdot \frac{1}{RBW} \cdot 10 = 1.92s \quad (6)$$

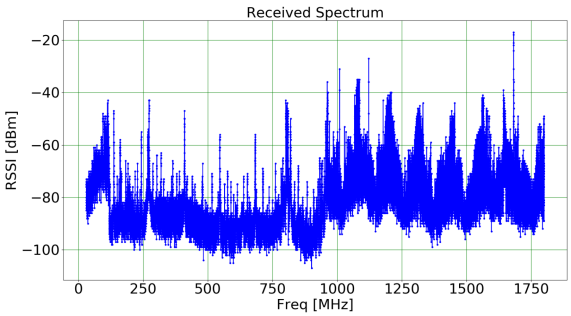

Fig. 6: The hole Band Received Spectrum.

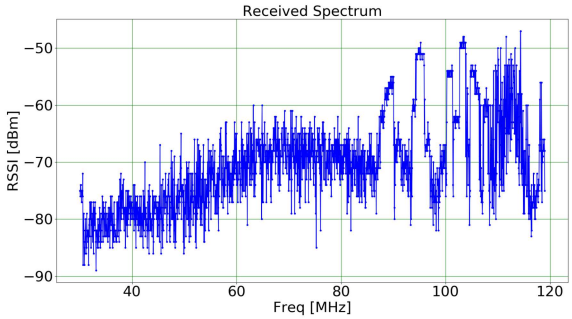

(a) The First Band Received Spectrum

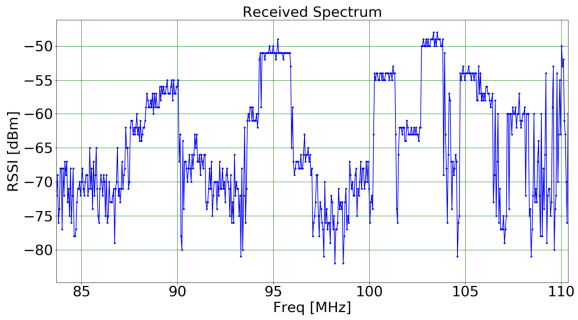

(b) FM Received Spectrum

Fig. 7: 2 Figures of The First Band Received Spectrum.

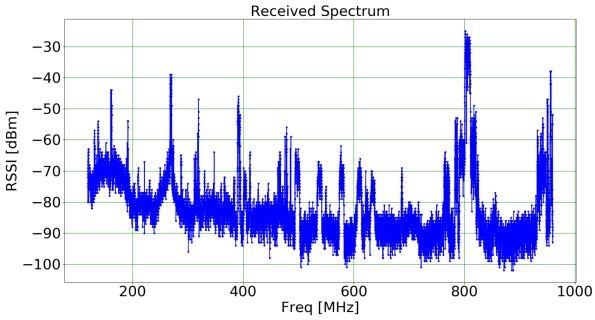

(a) The second Band Received Spectrum.

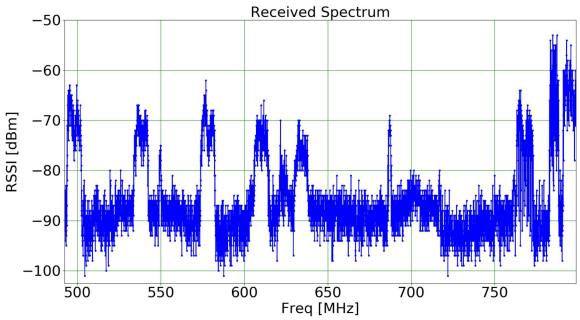

(b) DVB-T Received Spectrum.

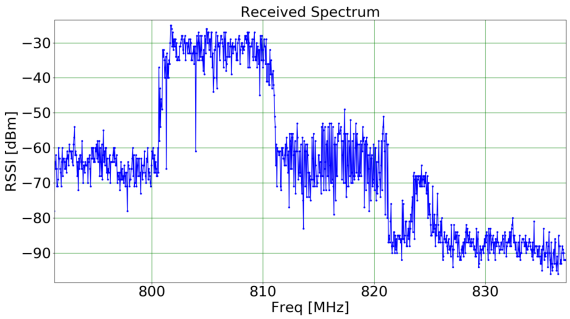

(c) LTE Received Spectrum.

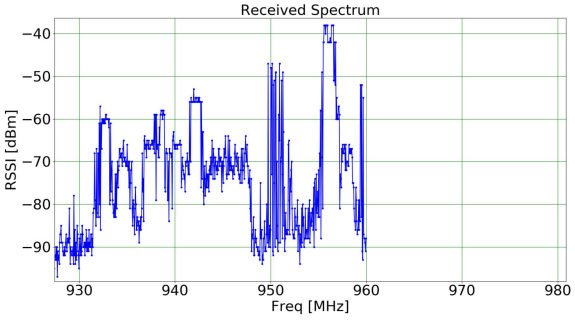

(d) GSM Received Spectrum.

Fig. 8: 4 Figures of The Second Band Received Spectrum.

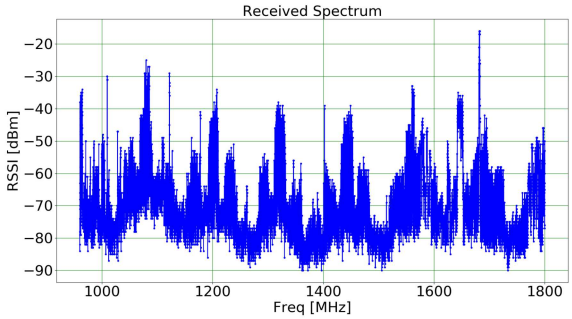

(a) The Third Band Received Spectrum.

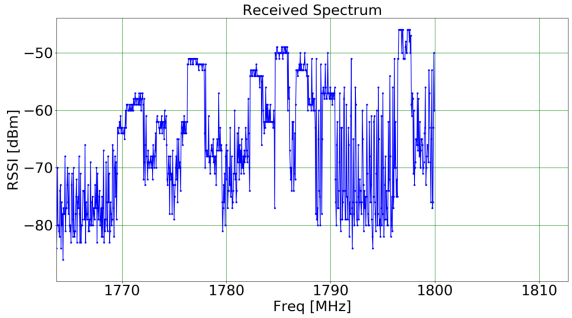

(b) UMTS Received Spectrum.

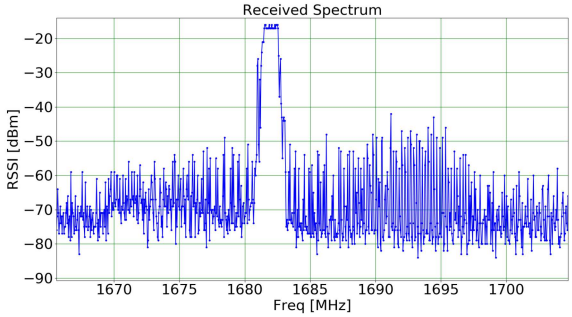

(c) The Second Harmonic of the Local Oscillator.

Fig. 9: 3 Figures of The Third Band Received Spectrum.

VI. CONCLUSION

The MRC-100 is currently being designed and will be launched in December 2022. According to the presented measurement results, the wideband spectrum monitoring system is presently operational in the laboratory and can measure RSSI (Received Signal Strength Indicator) values on three different RF bands. The system is sensitive enough and has enough dynamic range to be mounted as a scientific payload on the MRC-100 3-PQ (PocketQube) satellite to monitor RF smog in the upper HF band, FM band, VHF band, UHF band, LTE band, GSM band, 4G band, and UMTS band around the world in (LEO) orbit.

REFERENCES

[1] http://152.66.80.46/smog1/satellites.pdf
[2] Dudás, L., Varga, L., & Seller, R. (2009, August). The communication subsystem of Masat-1, the first Hungarian satellite. In Photonics Applications in Astronomy, Communications, Industry, and High-Energy Physics Experiments 2009 (Vol. 7502, pp. 184-193). SPIE. DOI: 10.1117/12.837484
[3] http://www.azurspace.com/images/0003429-01-01_DB_3G30C-Advanced.pdf
[4] https://www.silabs.com/documents/public/data-sheets/Si4464-63-61-60.pdf
[5] Dudás, Levente ; Gschwindt, András; Filling the Gap in the ESA Space Technology Education.
[6] Dudás, Levente ; Gschwindt, András; The Communication and Spectrum Monitoring System of Smog-1 PocketQube Class Satellite.
[7] Dudás, L., Pápay, L., & Seller, R. (2014, April). Automated and remote controlled ground station of Masat-1, the first Hungarian satellite. In 2014 24th International Conference Radioelektronika (pp. 1-4). IEEE. DOI: 10.1109/Radioelek.2014.6828410
[8] Takács, D., Markotics, B., & Dudás, L. (2021). Processing and Visualizing the Low Earth Orbit Radio Frequency Spectrum Measurement Results From the SMOG Satellite Project. INFOCOMMUNICATIONS JOURNAL, 13(1), 18-25. DOI: 10.36244/ICJ.2021.1.3

Miniaturized and modular flow chemical reactor for space applications

Ferenc Darvas, Balazs Buchholcz
ThalesNano Inc.
Zahony u. 7, 1031 Budapest, Hungary
ferenc.darvas@thalesnano.com

Gergo Mezohegyi
InnoStudio Inc.
Zahony u. 7, 1031 Budapest, Hungary
gergo.mezohegyi@innostudio.org

***Abstract*—Here we report the development of a miniaturized and modular flow chemical reactor which is able to perform a variety of important chemical reactions highly demanded by the pharmaceutical industry and intended to apply in microgravity environment in space. The design of the 2x0.5U sized flow synthesis equipment is based on prior investigations performed in non-miniaturized proof-of-concept reactors. In parallel to the assembly of the modular reactor, an external control unit was also designed and built, simulating the CPU, the control board and manifold system to be operated in-orbit. The unit is applicable for remotely controlled operation, making on-orbit synthesis feasible via ground control. Chemical synthesis tests have proved the feasibility of each reactor module for chemical operation on ground. Benzylic bromination as a photochemical transformation, S-benzylation for liquid-liquid reaction, Pd/C catalytic debenzylation for gas-liquid reaction and dichlorobenzaldoxime electrochemical transformation into nitrile were successfully carried out at high conversion rates in most cases. Although, it was originally developed onto ESA's Space Rider, the reactor prototype is also suitable for upscaling to in-space commercial production of active pharmaceutical ingredients.**

Keywords—space chemistry; flow reactor; drug discovery; chemical synthesis; in-space manufacturing

I. INTRODUCTION

In recent years, chemistry and drug discovery related research in space has gained rapidly increasing popularity [1]. This trend was mostly anticipated, considering that in parallel to the development of the space industry, chemistry related research and applications have become an important part of space research and also space manufacturing. More and more experiments are brought to space (especially to the International Space Station) these days with the aims for developing new materials, more sustainable technologies, but also novel chemical entities for discovery. Performing drug discovery in space offers a huge opportunity both for solving problems on Earth and also for future space travellers.

First, microgravity may offer more efficient reaction routes, even novel active pharmaceutical ingredients, which are difficult to synthesize on Earth. Microgravity formulation research results contributed to the FDA approval of the monoclonal antibody Keytruda® by Merck last year, used for treatment of patients with cervical cancer [2]. During the global SARS-CoV-2 epidemic, the first efforts have also been made on formulating anti-COVID compounds in space [3].

The pharma industry has recently indicated a growing interest in entering space and advancing its technologies or products in microgravity environment. A nice overview on the potential applications, recent scientific results and commercial perspectives of drug discovery in space has been given in the frame of a webinar series [4]. It is also surmised, however, that many related topics with high market-creating potentials are yet to be identified.

The second important area is the on-demand pharmaceutical production in space, which may provide just in time medication for long-term space travellers for avoiding the known pharmaceutical stability problems occurring in space [5]. Considering the implementation of pharmaceutical synthesis and manufacturing on-board, drug discovery in space will also require an advanced equipment that allows performing diverse chemical syntheses and transformations. For this purpose, flow chemical reactors are designated [6,7]. Flow technology is inevitable for space chemical synthetic applications, since conventional stirred reactors cannot be applied under microgravity. The design of a flow chemical system for operation in space is challenging, considering that fundamental aspects of constructing a flow reactor –for example, reagents properties, nature of chemicals involved, exotherm vs. endotherm reactions, pressure and temperature required– must follow the strict safety requirements of in-space applicability [8].

In 2019-2020, the first trials performing flow chemical reactions in space were carried out in the ISS National Lab, that recognized flow chemistry as an important application for future discovery and commercial efforts [9]. As up-to-date flow chemistry reactors can be operated under microgravity, and can completely be automated and remotely controlled while ensuring the required reaction parameters, efficient mixing of fluids and reliable operation. The precise controllability results in excellent reproducibility and safety, that makes flow chemistry a reasonable tool for space industrial and microgravity research applications.

Our company has developed a miniaturized and modular flow chemical reactor that is able to perform a diverse set of

chemical synthetic procedures, including photochemical, electrochemical and heterogeneously catalyzed reactions, and targeted for microgravity applications. The reactor design is feasible to in-line join analytical tools in order to execute chemical analyses in space. In the modular equipment, reaction types with high importance for the pharma industry can be performed. To the best of our knowledge, such modular, in-line remotely controllable equipment has not been applied in the space industry up to now. In this paper, the basic methodologies and achievements related to the miniaturized equipment development are presented and demonstrated with the results of the selected chemical syntheses.

II. Concepts and Methodology

The miniaturized chemical reactor was designed and built up with consideration to the following requirements: (i) the prototype reactor equipment shall fit the miniaturized laboratory environment (MOTI) originally conceptualized and to be provided by our international project partner SpacePharma [10]; (ii); operation of the chemical reactor shall be realized according to the conditions and limitations (e.g., in dimensions, power consumption etc.) formerly defined for the laboratory environment of our project partner; (iii) chemical testing of the modular reactor shall be performed by a self-developed control unit; (iv) the prototype reactor shall be remotely controllable, not requiring intervention by an astronaut when operating in space environment; (v) chemical reactions performed in the reactor, so as the reactor itself meet safety requirements of the space industry (especially of ESA's Space Rider vehicle); (vi) the modular chemical reactor prototype is able to execute diverse chemical reaction types in the different modules of the complex reactor.

Design and preparation of the miniaturized reactor system was based on preliminary comparative studies and testing in non-miniaturized proof-of-concept reactors. Different types of chemical reactions, all being considered highly important in the pharmaceutical industry, were selected as target reaction groups to be executed within the miniaturized system, namely, liquid-liquid reactions, gas-liquid reactions, heterogeneously catalyzed reactions, photochemical reactions, and also electrochemical reactions. The individual and miniaturized chemical reactors, able to perform these types of chemistries, were finally designed and assembled as components of a complex modular system (Fig. 1), from both practical and economic point of view. This way, the reactor unit as a whole can be integrated to the miniaturized laboratory, and all the five types of chemical reactions can be performed sequentially by the equipment, without the need of physical changing of an individual reactor. This will show numerous advantages during microgravity applications, for example, diverse types of chemical reactions can be studied at the cost of only one launch, but also, more types and numbers of chemical reactions and transformations can be performed in shorter time, thanks to the very compact reactor solution.

In parallel to the assembly of the modular reactor, an external control unit was also designed and built, simulating the CPU, control board and manifold system to be operated in-orbit. This unit made chemical testing and operation of the reactor prototype possible, which was a prerequisite before integrating the reactor into the MOTI environment. The software designed allows to run all the five different reaction types (with option for remote control), plus a cleaning cycle that shall be required between running two different reactions.

Prior to chemical testing, each reactor in the modular system and also the operating unit were tested and approved for physical and software operation (e.g., via pressure tests, leakage tests, electrical and control functions, liquid flow directions etc.).

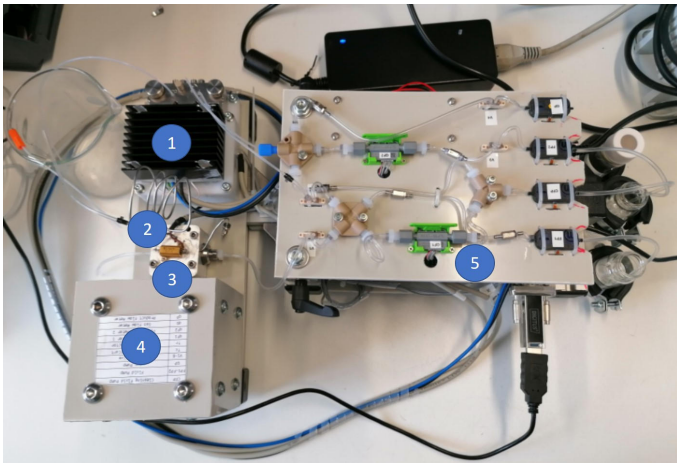

Fig. 1. Miniaturized modular chemical flow reactor prototype assembly: (1) chip reactor with LED built-in (allows to perform liquid-liquid, gas-liquid or photochemical reactions); (2) catalytic reactor (for heterogeneously catalyzed reactions); (3) electrochemical reactor; (4) spare space for analytical equipment; (5) operation (control) unit.

III. Results & Discussion

Preliminary chemical testing of the modular flow reactor with diverse solvents considered for later application resulted in exploring malfunction of a very few system components due to their insufficient solvent resistance. All these elements were changed and/or modified in order to ensure reliable and safe operation during the chemical syntheses.

A. *Liquid-liquid reaction*

The miniaturized flow reactor, developed for performing liquid-liquid reactions can ensure reaction types A + B > C or even A + B > C + D (latter one requiring a supplementary product separation unit). The chemical reaction takes place in a chip reactor assuring appropriate mixing of inlets and the required reaction parameters (T).

The S-benzylation carried out in the reactor was based on the flow phase transfer procedure described by Reichart et al. [11]. In this reaction, 2,4,6-trimethylthiophenol and benzyl bromide, both dissolved in dichloromethane, were reacted in the presence of potassium carbonate and tetrabutylammonium bromide, while the separated product was 2-(benzylsulfanyl)-1,3,5-trimethylbenzene (Fig. 2).

The synthesis, beside the chip reactor, was also performed in the reactor unit designed for heterogeneous catalysis, now filled with inert glass beads and at reduced flow rate, for comparative purposes only. Results are summarized in Table I.

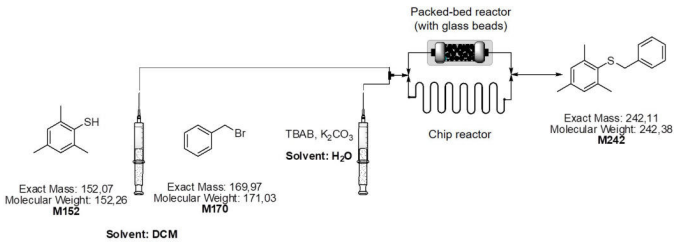

Fig. 2. Scheme for S-benzylation performed in the chip reactor and in inert packed-bed reactor.

As the results show, high conversion rates up to 80% could be achieved in the chip reactor at short residence times. The catalytic reactor design may be a good (and more economic) alternative to the chip-type solution for liquid-liquid reactions as well in case of syntheses not requiring higher flow rates. Both high activity of the thiophenol and efficient construction and mixing in the chip reactor contributed to such excellent conversions.

B. *Gas-liquid / catalytic reaction*

Both the chip reactor and catalytic reactor modules were designed and built to be applicable for also executing gas-liquid reactions. In the latter case, syntheses requiring heterogeneous catalysis can be performed. These modules, in case one of the inlets is a gas, are able to ensure the reaction type A(g) + B(liq) > C (liq).

The Pd/C catalytic debenzylation carried out in the miniaturized catalytic packed-bed reactor is based on the process described by Knudsen et al. [12]. N-BOC-O-benzyl-tyrosine was dissolved in EtOH/EtOAc mixture and reacted with H_2 using Pd/C catalyst in the packed-bed. The product was identified as BOC-L-Tyrosine (Fig. 3).

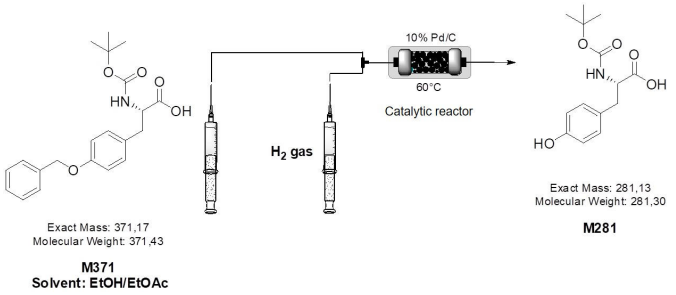

Fig. 3. Scheme for catalytic debenzylation performed in the catalytic packed-bed reactor.

TABLE I. SUMMARY OF RESULTS FOR S-BENZYLATION.

Reactor	Σ Flowrate (µL/min)	Residence time (min)	Temperature (°C)	M152 (%)	M170 (%)	M242 (%)	Conversion (%)
glass filled packed-bed reactor	48	2.5	40.0	5.0	13.8	81.2	94.2
chip reactor	200	5.0	50.0	6.1	13.4	80.5	93.0
	400	2.5	50.0	13.0	13.7	73.3	84.9

Table II. shows results of the synthesis, including conversions between 42-62% achieved at altered flow rates. Unexpectedly, following the enhancement of flow rate and then setting it back to the initial value resulted in a higher conversion. Moreover, in a separate experiment at a fixed flow rate, the otherwise high conversion values presented a relatively large standard deviation. This can be explained by omitting the use of a H_2 mass flow controller in the set-up, which was considered too robust for integrating it into the miniaturized device. The reactor technology itself, however, was approved to be a safe, highly efficient and promising method for making gas-liquid reactions under microgravity executable.

C. *Photochemical reaction*

The design and assembly of the photochemical flow reactor was based on the chip reactor set-up. During the photochemical reaction, a LED light source is irradiating the total liquid flow passing through the chip reactor. The cooling of the reactor was ensured by an external heat sink for the chemical tests (the MOTI environment was about to include Peltier coolers). The photochemical module can ensure the reaction types A > (hν) B or A + B > (hν) C.

Benzylic bromination was selected as a representative reaction to evaluate efficiency and feasibility of the photochemical reactor module. The reaction was based on the work of Edwards et al. [13]. In this reaction, methylacetophenone and N-bromosuccinimide, both dissolved in MeCN/AcOH (1:1) were reacted at LED wavelength of 450 nm to produce a mixture of monobromine and dibromine compound (Fig. 4). The latter compound, being a by-product, required a selective debromination procedure for analytical purposes. The valuable product compound was 1-[4-(bromomethyl)phenyl]ethan-1-one.

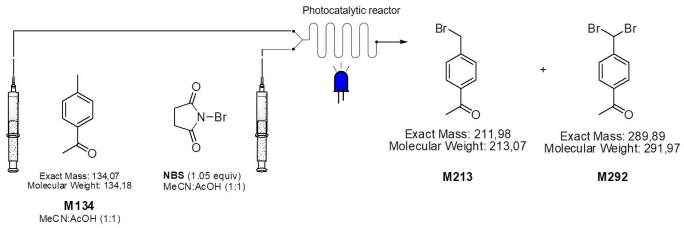

Fig. 4. Scheme for benzylic bromination performed in the photochemical reactor.

In the experiment, the effect of residence time, temperature and LED intensity on conversion were studied. Table III. indicates that the applied range of flow rate had minor effect on conversion, that remained high (up to 89%) at all residence time tested. Selectivity, however, could be slightly increased at lower flow rates. Increasing the temperature resulted in somewhat lower conversion values and selectivity. Varying the LED intensity, however, gave unexpected results with

measuring the lowest conversion (80%) and also selectivity (66%) at maximum intensity (100%).

TABLE II. SUMMARY OF RESULTS FOR CATALYTIC DEBENZYLATION.

Experiment No.	Liquid flowrate (µL/min)	Gas flowrate (µL/min)	Temperature (°C)	M371 (%)	M281 (%)	Conversion (%)	EtOAc (%)	PhMe (%)	Other (%)
1	250	1000	60.0	48.2	36.5	42.2	11.8	1.8	1.7
2	500	1000	60.0	70.6	16.1	18.3	10.9	1.0	1.4
3	250	1000	60.0	28.5	51.3	62.0	14.1	3.1	3.0

TABLE III. SUMMARY OF RESULTS FOR BENZYLIC BROMINATION.

Experiment No.	LED intensity (%)	S Flowrate (µL/min)	Residence time (min)	Temperature (°C)	M134 (%)	M213 (%)	M292 (%)	Conversion (%)	Selectivity (%)	Other (%)
1	50	100	10.0	37.3	10.8	72.0	15.5	89.2	80.7	1.7
2	50	133	7.5	37.3	12.7	67.8	17.6	87.3	77.7	1.9
3	50	200	5.0	37.3	14.7	62.6	20.7	85.3	73.4	2.0
4	50	400	2.5	37.3	16.7	57.6	22.8	83.3	69.1	2.9
5	50	1000	1.0	37.3	12.4	67.4	18.0	87.6	76.9	2.2

TABLE IV. SUMMARY OF RESULTS FOR NITRILE SYNTHESIS.

Experiment No.	Current (mA)	Potential (V)	Flowrate (µL/min)	Concentration (mM)	Operation time (min)	M190 (%)	M172 (%)	Conversion (%)	Selectivity (%)	M188 (?) (%)	Other (%)
1	4.8-5.0	7.6	22	121	20-22	82.0	8.3	18.0	46.1	4.5	5.2
2	5.0	5.9-6.9	22	121	40-42	87.1	6.4	12.9	49.6	3.0	3.5
3	5-5.2	7.6	22	121	66-68	81.4	8.5	18.6	45.7	4.5	5.6
4	5-5.2	7.8-8.1	22	121	88-90	83.4	10.6	16.6	63.9	2.8	3.2
5	5.0	6.0-10	22	121	20-90	84.1	9.7	15.9	61.0	3.3	2.9

D. Electrochemical reaction

Efficacy of the miniaturized electrochemical cell was demonstrated with the example reaction of domino oxidation-reduction of 2,6-dichloroenzaldoxime (Fig. 5), described by Gütz et al. [14].

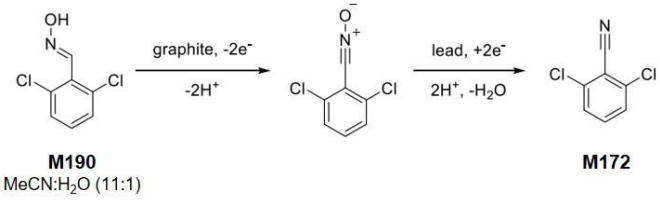

Fig. 5. Scheme for nitrile synthesis from aldoxime in the electrochemical reactor.

The miniaturized electrochemical reactor was proved to be feasible for executing electrochemical transformations (Table IV.). The conversion values and yields achieved in the given synthesis were found somewhat lower to the ones of the reference study. This may be explained by omitting the use of methyl-tri-propylammonium methylsulfate, served as electrolyte for optimized conditions in the reference work. The cell's performance remained stable during its continuous operation for 90 min. Reduced flow rates (to half) did not result higher conversion values. The electrochemical reaction, in general is strongly dependent on several operation parameters, such as current density, liquid temperature and pressure, electrode materials and concentration of reactants.

IV. CONCLUSIONS

The developed miniaturized and modular flow chemical reactor has proved to be feasible to execute a wide range of chemical syntheses with high efficiency. The results show that high conversions and yields could be achieved for diverse pharmaceutical syntheses in the chip reactor, catalytic reactor and photochemical reactor, while the electrochemical module and cell will require further research and optimization for their elevated performance. The developed operation unit allows remote control of chemical transformations performed in the reactor, making on-orbit synthesis feasible via ground control. Although originally designed onto the Space Rider for demonstrative and research purposes, the reactor equipment prototype, following its space qualification, can also be feasible for upscaling for diverse commercial purposes, including in-space pharmaceutical manufacturing, production of (new) materials and fuels on orbit, chemical processing for asteroid and planet mining, or even life support on Mars (e.g., CO_2 transformation to valuable materials).

ACKNOWLEDGMENT

The authors express their gratitude for the grant No. 2019-2.1.10-TÉT-IL-2019-00002 provided by the National

Research, Development and Innovation Office. The authors furthermore thank Dr. Gellert Sipos for his expertise and helpful assistance in chemical testing procedures.

REFERENCES

[1] R. Jones, F. Darvas and Cs. Janáky, "New space for chemical discoveries", Nature Reviews Chemistry, Vol.1 (Article No.0055), pp.1-3, 2017.

[2] P. Reichert, W. Prosise, T.O. Fischmann, G. Scapin, C. Narasimhan, A. Spinale, R. Polniak, X. Yang, e. Walsh, D. Patel, W. Benjamin, J. Welch, D. Simmons and C. Strickland, "Pembrolizumab microgravity crystallization experimentation", NPJ Microgravity, 5, 28, pp.1-8, 2019.

[3] G. Mezohegyi, B. Buchholcz, I. Puskas, L. Szente, T. Sohajda and F. Darvas, "Effect of microgravity on COVID-19 drug formulation on ISS", 10th Annual International Space Station Research and Development Conference (Technical Sessions), 16-18 August 2021.

[4] https://drugdiscoveryinspace.com/ (accessed: 25 March 2022).

[5] P. Mehta and D. Bhayani, "Impact of space environment on stability of medicines: Challenges and prospects", Journal of Pharmaceutical and Biomedical Analysis, 136, pp.111-119, 2017.

[6] F. Darvas, Gy. Dormán and V. Hessel, V. (eds), "Flow chemistry – Volume 1: Fundamentals", Berlin, De Gruyter, 2014.

[7] G. Mezohegyi and F. Darvas, "Trends in space chemistry: emerging markets and potential applications", Reinventing Space Conference, Belfast, 12-14 November 2019.

[8] G. Sipos, T. Bihari, D. Milánkovich and F. Darvas, "Flow chemistry in space – A unique opportunity to perform extraterrestrial research", Journal of Flow Chemistry, 7, pp.151-156, 2017.

[9] https://www.issnationallab.org/iss360/boston-university-flow-chemistry-facilitation-spacexcrs20/ (accessed: 25 March 2022).

[10] https://www.space4p.com/ (accessed 25 March 2022).

[11] B. Reichart, C.O. Kappe and T.N. Glasnov, "Phase-transfer catalysis: Mixing effects in continuous-flow liquid/liquid O- and S-alkylation process", SYNLETT, 24, pp.2393-2396, 2013.

[12] K.R. Knudsen, J. Holden, S.V. Ley and M. Ladlow, "Optimisation of conditions for *O*-benzyl and *N*-benzyloxicarbonyl protecting group removal using an automated flow hydrogenator", Advanced Synthesis & Catalysis, 349(4–5), pp.535-538, 2007.

[13] H.E. Bonfield, J.D. Williams, W.X. Ooi, S.G. Leach, W.J. Kerr and L.J. Edwards, "A detailed study of irradiation requirements towards an efficient photochemical Wohl-Ziegler procedure in flow", ChemPhotoChem, 2, 10, pp.938-944, 2018.

[14] C. Gütz, A. Stenglein and S.R. Waldvogel, "Highly modular flow cell for electroorganic synthesis", Organic Process Research & Development, 21, 5, pp.771-778, 2017.

Using quantum algorithms for Earth Observation data processing

Doaa Subhi
Department of Networked Systems and Services
Budapest University of Technology and Economics,
Műegyetem rkp. 3., H-1111 Budapest, Hungary
alnuaim@hit.bme.hu

Laszlo Bacsardi
Department of Networked Systems and Services
Budapest University of Technology and Economics,
Műegyetem rkp. 3., H-1111 Budapest, Hungary
bacsardi@hit.bme.hu

***Abstract*— Big data is collected these days from various sources including sensors and cameras and contains important information about space, weather, medical application, industrial application, etc. Such information requires processing and storage memory, the limited ability of classical computers makes it hard to deal with such a huge amount of data. Quantum algorithms offer revolutionary solutions in various domains which require complex computational steps.**

In our paper, we introduce selected quantum algorithms that can be run on quantum computers soon to support the data handling process for images arriving from the Earth Observation satellite. We briefly present a potential application area named quantum image processing (QIP) which could be utilized to enhance the data processing operation while handling Earth Observation data. The novel idea of QIP is aimed to apply principles of quantum physics such as superposition, entanglement, and parallelism to image processing applications. instead of using classical algorithms. This will be able to solve many problems, reduce computational complexity, and exponentially speed up compared to the classical one, no matter how large the amount of data we deal with. Future's quantum computer will be able to perform the algorithms of QIP such as image representation, detection, etc., and break the classical limitation of calculation.

Keywords*— *quantum computers; quantum algorithm; image processing.

I. INTRODUCTION

Big data is collected these days from various sources including sensors and cameras and contains important information about space, weather, medical application, industrial application, etc. Such information requires processing and storage memory, the limited ability of classical computers makes it hard to deal with such a huge amount of data.

Quantum computers are powerful tools in big data-related data processing utilizing the phenomenon of quantum physics such as superposition, entanglement, and parallelism [1]. Due to these properties' quantum computers provided high-speed algorithms to process data and memory based on using quantum registers. From the viewpoint of quantum computing, we name the nowadays used techniques as classical (e.g., classical computers, classical algorithms, etc.).

In our survey paper, we introduce how quantum computers can help achieve higher performance in big data handling by utilizing the power of quantum parallelism. We are focusing on optical data processing which has an important role in Earth Observation (EO). We introduce quantum image processing algorithms which can outperform the classical image processing algorithm, offering faster response time in any service which is using data based on optical images.

Quantum image processing is an important branch of quantum information and computation theory, it is a promising technology that will come up with better images in terms of resolution, memory, and complexity. QIP has an exponential storage advantage if compared with the classical one, representing a square quantum image requires $(\lceil \log_2 N \rceil + \lceil \log_2 N \rceil + l)$ qubits, while classical needs (N x N x bit depth) bits [2]. Based on quantum Fourier transform and quantum image compression (QIC) different algorithms are introduced recently to represent, store, and retrieve images by using quantum computers.

.

II. QUANTUM ALGORITHM

Feynman [3] was the first who suggested using quantum computers based on the principles of quantum physics in 1982. Quantum computers are more powerful than classical computers, where the processors of classical ones consist of a transistor (semiconductor material), which could reach its physical limitation in the next few years. According to Moore's law [4], we will reach the limit of classical transistors. To be able to further increase the calculation capacity, we need to apply the laws of quantum physics and build quantum computers. Quantum computers are based on quantum bit (or qubit in short). A qubit can be represented by any two-level quantum system such as the spin of an electron, trapped ion, photon, or atom. These qubits are represented in the bases of |0> and |1>, in a so-called superposition form:

$$|\psi\rangle = \alpha|0\rangle + \beta|1\rangle \qquad (1)$$

where α and β are complex numbers and |α|^2+|β|^2=1.

Quantum bit is linked with two-dimensional Hilbert space which provided its ability to be in the superposition state of 0 and 1. The pure state of a qubit is described by a unit vector

belonging to a two-dimensional complex Hilbert space as in equation 1.

In quantum computers, the qubit represents the basic information unit that meets the binary bit in the classical. A qubit can be in superposition in two states at the same time while the classical binary bit cannot be on both states simultaneously (i.e., if one entry has 1, then the other will be zero). Here the information bits are measured by the probability of the possible states, where the memory consist of n bits of information has 2n states represented by a probability vector. A qubit can be defined as a higher-dimensional quantum system that is described by a dimensional Hilbert space Hd and referred to as qudits.

Bloch sphere is a geometrical representation used to represent the quantum states, qubits can be represented at any point of the sphere surface while classical bits could be represented only by the north or south pole of the sphere. Quantum computers have applications in different fields such as cryptography, optimization problems, and image processing, because of their ability to solve the problems that face classical computers in such fields.

Deutsch [5] suggested using quantum algorithms instead of classical ones. Different quantum algorithms are suggested to deal with various trends such as machine learning, image processing, classification, factorization, and searching. The most important advantage of such algorithms is the required time complexity and storage memory lass than classical one such as quantum algorithm suggested by [6], which find larger Walsh coefficients with time query equal to $O\left(\frac{\log\frac{1}{\delta}}{\epsilon^4}\right)$ while classical one takes a $poly\left(n,\frac{1}{\epsilon}\log\frac{1}{\delta}\right)$.

Images are one the important sources of information because of their massive applications in various fields such as medical, industrial, weather, etc. Using of quantum mechanics for image reorganization was first suggested by [7] who focuses on the use of quantum mechanics to realize orthogonal images, but a major role of research in quantum image processing is assigned to [8], which suggests using quantum mechanics in images storage and retrieval, then compare with classical methods. Using quantum mechanics principles for image processing provided us with unique properties such as higher computing speed, ensuring security, and reduced memory requirement. These improvements are due to the quantum computers attribute illustrated above and using of qubit instead of classical bits. OIP could perform image processing such as image storage, retrieval, representation, encryption, segmentation, etc. better than the classical one.

In the classical representation of images, images are represented by using matrices, and each value is represented by a pixel. While for quantum representation there are two main representation methods state amplitude-based and basic state representation. In amplitude representation, the value of the pixel is represented by the amplitude of the qubit such as in the FRQI algorithm [2], while for base state representation pixels values are stored in the state of the qubit sequence such as in the NEQR algorithm [9]. There are different other methods to store and retrieve quantum images such as entangled quantum sequence [10] and others.

III. Quantum Image Processing

Quantum algorithms can be used to help the image processing which is a typical step in Earth Observation. Image processing based on quantum physics is named Quantum Image Processing (QIP), which deals with image storage, retrieval, security, etc., by using quantum computing instead of the classical one. The pictures are two-dimensional matrices that are represented in the memory by a quantum bit called grid qubit. In the next subsections, we introduce selected algorithms which are compared in Table I.

A. Quantum Image Processing Representation

- FRQI is the most used image representation method, it is represented the quantum image as is the normalized state [2]. Use unitary transform to express its state by three operators, first for color information, second for the color position, and third for both color and position. The drawback of this approach it is disabled to retrieve the original classical image because of the probability amplitude probability of the quantum state. Recently, an enhanced method based on FRQI suggested by Norhan and co-authors [11], enhances the time complexity of the FQRI Avoid combining SI and CGS units, such as current in amperes and magnetic field in oersteds. This often leads to confusion because equations do not balance dimensionally. If you must use mixed units, clearly state the units for each quantity that you use in an equation.

- Novel Enhanced Quantum Representation (NEQR). NEQR suggested 2013 [9], that it is based on the basic state to encode pixels' intensity value inside the image. NEQR solves the FRQI, by recovering the exact original image by using a single measurement only. Only one problem with this type it is used for square images only. Recently an enhanced ENQR (ENQR) was introduced by Norhan and co-authors [11], which enhances time complexity and has less quantum cost.

- Multi-channel representation for quantum images (MCQI). MCQI works based on FRQI and uses R, G, and B channels to encode color square quantum images, it encoded color information by using angle parameters [12]. In this approach three qubits are used to encode the color information, making the design of the color image easier and has less complexity. In the same direction flexible representation of color images suggested by [13] uses only a single bit to represent the color images.

- Caraiman's quantum image representation model (CQIR): In the CQIR approach [14], 2m possible color can be expressed in a superposition state. The retrieval of the image can be applied using a deterministic way instead of a probabilistic such as FRQI. This approach provided fast and efficient color image operation because it isn't using simple quantum gates.

- Quantum normalized amplitude-based image processing (QNAIMP): QNAIMP approach is suggested by [15], an image is represented by a two-dimensional matrix of m-qubit row and n-qubit column vectors. The tensor product of the row location and column-location vector results in a 2-D quantum state of a pixel in the Liouvillian space. Hence, m + n qubits without additional qubits will be required to represent quantum images.
- Quantum entangled image processing (QEIP): In the QEIP method [10] an entangled state is used to store a binary image in a quantum system. An image is stored as a two-dimensional array with two parameters x and y, which contain a grid point. This method has a special property over others that can represent rectangular images.

Recently different methods are suggested to represent and store the images by applying quantum algorithms such as Optimized quantum representation for color digital images (OCQR) [16]. A new quantum representation model of color digital images (QRCI) [17] which is based on entangled qubit sequence to represent the image. Double quantum color images encryption scheme DQRCI [18], etc.

TABLE. I: COMPARISON OF DIFFERENT QIP METHODS

QIP representation	Method used	Algorithm	Processing type	Image type/shape	Storage memory / no. of qubits needed	Time complexity
FRQI [2]	Normalize state	Quantum image compression (QIC	Image storage, retrieval	grayscale images/ square images only	A single bit is used to represent color information	$O(2^{4n})$
EFRQI [11]	Normalize state	Same as FRQI	Image storage, retrieval	Color images/square images only		$O(2^{4n})$
NEQR [9]	Basic state	Same as FRQI	Image storage, retrieval	Grayscale images only/square images only	2n + 8 qubits	$O(2qn2^{2n})$
ENEQR [11]	Basic state	Same as FRQI	Image storage, retrieval	Grayscale images	2n+1 qubits	$O(2n2^{2n})$
MCQI [12]	Normalize state		Image storage, retrieval	for all image types	3-qubits to store $2^n \times 2^n$	
CQRI [14]	Finite deterministic		Image storage, retrieval segmentation	2 m possible colors (m+2n)- qubit register	2 m possible colors (m+2n)- qubit register	
QNAIMP [15]	Normalize state		Storage and retrieval	For all image types	(m+n) qubits	
QEIP [10]	Entangled quantum sequence	Grover's quantum search algorithm	Image storage, retrieval, histogram, segmentation	Binary images only	N-qubits	O(n)

B. Security base technologies of the QIP

- Watermarking and authentication of quantum images WaQI Watermarking is a process by which the copyrights of an image was protected and authenticated which is represented while the fixed parameters are used for the other schemes' embedding process. Moreover, dynamic watermarking can be classified into wavelet transform watermark and Hadamard transform-based watermarking. Most of the quantum watermarking schemes are applied for the multi-channel FRQI representation, the adoption of MCQI representation for the carrier and watermark images facilitates the protection of colored quantum images and improves the capability of watermarked images to withstand malicious attacks.
- Quantum image encryption algorithms: Information sharing, and other communication types are needed to be encrypted to stop eavesdroppers and keep the information secure, especially in military communication, politics, and medical applications. Most algorithms of quantum images focus on two parameters position information and color information. The position-based algorithms are the Hilbert transform, Arnold transforms, and Fibonacci transform.
- Quantum image steganography: Steganography is the technique that focuses on hiding secret information. A Moire pattern-based NEQR image steganography strategy [19], designed as an algorithm work with a logo that may be visible or invisible. Reference [20] suggests the first quantum image security protocol, which is based

on quantum cosine transform to build an invisible watermarking. Generally, there are two types of watermarking techniques first based on fixed parameters, and the other based on a dynamic vector, dynamic vector is used to control the embedding strength quantum circuit to hide a binary image into a grayscale image. Then an enhanced version based on two blind LSB algorithms [21] based on NEQR representation, two types of this algorithm plain standard (used message bits to substitute for the pixels' LSB directly) and block LSB (embeds a message bit into several pixels that belong to one image block).

C. *Quantum Image recognition*

Quantum image recognition: image recognition is the ability of the machine to recognize people, objects, writing, etc in the image. The importance of such a field of research leads to an investigation of very wide algorithms to make the process more precise and better work. In 1997, [7], suggest using quantum mechanics to enhance image recognition. One of the important images that deal with is the medical one, [22] suggests a new algorithm based on quantum BP neural network (QBP) based on quantum particle swarm optimization (QPSO), that recognizes the pneumonia image

IV. CONCLUSION

In our paper, we introduced selected quantum algorithms that can be run on quantum computers soon to support the data handling process for images arriving from Earth Observation satellites. Quantum mechanics can be applied to image processing to attain high-performance image representation, storage, segmentation, etc. In this article, we reviewed some important algorithms used by the quantum system to represent images. Some security approaches including image watermarking and steganography techniques are presented based on using of quantum computing.

ACKNOWLEDGMENT

The research has been supported by the Ministry of Innovation and Technology and the National Research, Development, and Innovation Office within the Quantum Information National Laboratory of Hungary. L. Bacsárdi thanks the support of the János Bolyai Research Scholarship of the Hungarian Academy of Sciences.

REFERENCES

[1] S. Imre, F. Balazs, "Quantum computing and communications: An engineering approach", Wiley, 2005.

[2] P.Q. Le, F. Dong, and K. Hirota, "A flexible representation of quantum images for polynomial preparation, image compression, and processing operations" Quantum Inf Process 10, pp.63–84, 2011. https://doi.org/10.1007/s11128-010-0177-y.

[3] R. P. Feynman, "Simulating Physics with Computers", International Journal of Theoretical Physics, 21, pp.467–488, 1982. https://doi.org/10.1007/BF02650179.

[4] G. E. Moore, "Cramming more components onto integrated circuits," Electronics, vol. 38(8), pp. 114–117, 1965

[5] D. Deutsch, "Quantum theory, the Church-Turing principle and the universal quantum computer", Proceedings of the Royal Society of London, series A 400, pp. 97-117, 1985. https://doi.org/10.1098/rspa.1985.0070.

[6] Hongwei Li, " Quantum algorithms for the Goldreich–Levin learning problem", Quantum Information Processing, vol. 19(11), 2020. https://link.springer.com/article/10.1007/s11128-020-02839-7.

[7] A. Y. Vlasov, " Quantum Computations and Images Recognition", arXiv: Quantum Physics, 1997.

[8] S. E. Venegas-Andraca and S. Bose, "Storing, Processing and Retrieving an Image Using Quantum Mechanics," Proceedings of SPIE Conference of Quantum Information and Computation, 5105, pp. 134-147,2003. doi: 10.1117/12.485960.

[9] Y. Zhang, K. Lu, Y. Gao and M. Wang, "NEQR: a novel enhanced quantum representation of digital images," Quantum Inf. Process, August 2013. DOI 10.1007/s11128-013-0567-z.

[10] S. E. Venegas-Andraca,, J.L. Ball, "Processing images in entangled quantum systems", Quantum Inf Process 9, pp. 1–11, 2010. https://doi.org/10.1007/s11128-009-0123-z.

[11] N. Nasr, A. Younes, and A. Elsayed," Efficient representations of digital images on quantum computers", vol. 80, pp. 34019–34034, August 2021.

[12] Bo Sun, A. M. Iliyasu, F. Yan, F. Dong, and K. Hirota, "An RGB Multi-channel representation for images on quantum computers", Journal of Advanced Computational Intelligence and Intelligent Informatics, vol. 17(3), pp 404-415, 2013. DOI:10.20965/jaciii.2013.p0404.

[13] L. Panchi and L. Xiande, "Color image representation model and its application based on an improved FRQI", vol. 16, 2018.

[14] C. S. Manta," Image segmentation on a quantum computer", Quantum Inf Process 14, pp. 1693–1715, 2015.

[15] M. Srivastava, S. Roy-Moulick, and P. K. Panigrahi, "Quantum image representation through Two-Dimensional quantum states and normalized amplitude", IEEE SIGNAL PROCESSING LETTERS, July 2015.

[16] K. Liu, Y. Zhang, K. Lu, and X. Wang, "An optimized quantum representation for color digital images", Int J Theor Phys vol. 57(10), pp.:2938–2948, October 2018.

[17] L. Wang, Q. Ran, J. Ma, S. Yu, and L.Tan, "QRCI: a new quantum representation model of color digital images" Opt Commun, vol. 438, pp.147–158, 2019.

[18] L. Wang, Q. Ran, and J Ma, "Double quantum color images encryption scheme based on DQRCI", Multimed Tools Appl, Vol. 79(9), pp.6661–6687, 2020.

[19] N. Jiang and L. Wang, "A Novel Strategy for Quantum Image Steganography Based on Moire Pattern", International Journal of Theoretical Physics, vol. 54(3).2015. DOI: 10.1007/s10773-014-2294-3.

[20] A. M. Iliyasu, F. Yan and K. Hirota, "Metric for Estimating Congruity between Quantum Images", Entropy, vol. 18(10), p.360, 2016. https://doi.org/10.3390/e18100360, 2016.

[21] N. Jiang, N. Zhao and L. Wang, "LSB Based Quantum Image Steganography Algorithm", International Journal of Theoretical Physics ,vol. 55, pp.107–123, 2016.

[22] D. Yumin, M. Wu, and J. Zhang, "Recognition of Pneumonia Image Based on Improved Quantum Neural Network", IEEE Acess, vol.8, pp. 224500 – 224512, 2020.

Promoted and organized by

BME Faculty of Electrical Engineering and Informatics

Hungarian Astronautical Society

Sponsors

Budapest University of Technology and Economics

Ministry of Foreign Affairs and Trade

Partners

BME Cosmos Circle

Space Generation Advisory Council

H-SPACE 2022

The 1st International Conference on Research, Technology and Education of Space was the opening event of the conference series. It was held on February 13, 2015.

The 2nd International Conference on Research, Technology and Education of Space was held on February 25-26, 2016.

The 3rd International Conference on Research, Technology and Education of Space was held on February 9-10, 2017.

The 4th International Conference on Research, Technology and Education of Space was held on February 15-16, 2018.

The 5th International Conference on Research, Technology and Education of Space was held on February 27-28, 2019.

The 6th International Conference on Research, Technology and Education of Space was held on February 26-27, 2020.

The 7th International Conference on Research, Technology and Education of Space was held on April 7-8, 2022.

H-SPACE 2024, the 8th International Conference on Research, Technology and Education of Space' is planned to be organized in February 2024 in Budapest, Hungary.

The Call for Papers will be available from September 1, 2023 on the http://space.bme.hu website.